Numerical and experimental study of the seakeeping performance for a novel fish farming vessel considering nets

Ziqi Liu[1,2], Jintao Zhang[1], Wei Huang[3], Binbin Li[1]*

[1]*Shenzhen International Graduate School, Tsinghua University, Shenzhen 518055, China*
[2]*China Offshore Engineering & Technology Co., Ltd., Shanghai 200011, China*
[3]*School of Civil Engineering, Sun Yat-Sen University, Guangzhou 510275, China*

ARTICLE INFO

ABSTRACT

To improve the economic feasibility of offshore aquaculture, this study proposes a novel concept of fish farming vessel which is retrofitted by an old bulk carrier. Large open farming tanks has been created by replacing the side hull plates with rigid metal nets and retaining the transverse bulkhead. The seakeeping performance of the vessel is evaluated through numerical simulations which are validated against experimental results. A numerical model based on the potential flow based boundary element method is developed using panel elements for the hull and dipole elements for the nets. The effects of net solidity ratio and wave slope variation on seakeeping performance are analyzed. Results show that increasing solidity ratio leads to higher peaks near the natural frequencies in the Response Amplitude Operators (RAOs). Besides, the installation of net generally reduces RAOs due to wave energy dissipation through nets and decreased wave excitation. Comparisons with experimental results from free decay, regular waves, and white noise waves tests demonstrate good agreement in terms of natural frequencies and trends of RAOs. Discrepancies in natural frequencies, especially in pitch motion, are attributed to the underestimation of added mass in the numerical model. The findings validate the feasibility of using dipole elements to represent net structures and underscore the importance of accounting for wave slope in seakeeping analysis of net-integrated offshore structures.

1. Introduction

With the continuous growth of the global population and increasing demand for marine protein, aquaculture has emerged as a key solution to address food supply and resource pressure. Marine aquaculture production is projected to reach 74 million tonnes by 2050, approaching the output of marine capture fisheries and becoming one of the primary sources of seafood [1]. To secure larger farming areas, improved quality of seafood, and reduced pollution impacts on coastal urban areas, the aquaculture industry is steadily moving towards deeper and more remote marine environments. However, the harsh offshore conditions pose significant challenges to traditional nearshore net cage systems, which are often inadequate for such

---

environments. In response, the concept of offshore aquaculture structures has been proposed and applied, offering more robust configurations capable of withstanding severe sea states. Among them, fish farming vessels represent a promising direction by integrating fish farming compartments with conventional ship hull structures, allowing for easier design, construction, and potential self-propulsion for site relocation. In recent years, the design and application of such vessels have gained increasing attention as a feasible solution for offshore aquaculture deployment.

(a) Havfarm 1
(Courtesy of Nordlaks)

(b) Bay Area Lingding
(Courtesy of Zhuhai Ocean Development Group Co)

(c) Guoxin 2-1
(Courtesy of Qingdao Conson Group)

(d) Senhai Pioneer
(Courtesy of Senhai Muge Marine Technology)

Fig. 1 Fish farming vessels

Fish farming vessels are generally categorized into fully permeable, closed and semi-open types according to the level of water exchange between the aquaculture tanks and the surrounding seawater. A representative example of fully permeable fish farming vessel is Havfarm 1 in Figure 1 (a), which features a steel truss structure approximately 385 m in length and 59.5 m in width. It contains six aquaculture cages, each with dimensions of 60 m in depth and same length and width, providing a total capacity of 10,000 t for salmon [2]. Another application is the Bay Area Lingding vessel in Figure 1 (b). With a length of 155.8 m, a beam of 24 m, and a maximum draft of 20 m, the structure is supported by 15 square columns and enclosed by nets to form 12 aquaculture tanks, with an expected annual production capacity of 5,000 t. Notably, the vessel is equipped with two 3,600 kW rudder propeller units, enabling it to navigate autonomously, select farming locations, and avoid harsh environmental conditions such as typhoons [3]. For the fish farming vessel with closed aquaculture tanks, a notable case is Guoxin 2-1, an upgraded version of Guoxin 1 launched in 2022. With a length of 100 m and a beam of 30 m, the vessel is capable of farming up to 3,600 t of high-value fish such as large yellow croaker and amberjack [4]. Water exchange between the inside and outside of the vessel is managed via dedicated treatment systems, effectively reducing the risk of disease transmission. Meanwhile, sloshing in the internal tanks is the key issue that needs to be addressed for this type of vessel, similar to LNG carriers [5, 6]. For semi-open fish farming vessels, Senhai Pioneer is a representative example.

It was converted from a 225 m long Panamax-class bulk carrier originally built in 1996. The vessel is capable of farming up to 2,800 t of fish. Notably, openings were added to the vessel's sides and bottom, allowing direct exchange between internal tank water and the surrounding seawater, thereby maintaining suitable farming conditions while utilizing the existing ship structure [7].

While the aforementioned fish farming vessels offer effective solutions for deep-sea aquaculture, they are generally associated with extremely high construction costs, which negatively affect the economic viability of the industry. For instance, the Havfarm 1 project had a reported cost of 1 billion NOK (95 million USD), while the Bay Area Lingding vessel required a total investment of 260 million CNY (36 million USD). Also, the Guoxin 2-1 vessel, the upgraded version of Guoxin 1, involved an investment of 610 million CNY (85 million USD), which is 50% higher than its predecessor. Compared to those newly built vessels, the Senhai Pioneer demonstrates that converting aged bulk carriers can significantly reduce project costs and eliminate long construction periods. Besides, the converted vessel retains the original ship's capability to withstand harsh environmental conditions such as typhoons. Notably, there are currently around 1,500 bulk carriers of similar age worldwide, which could be retrofitted for aquaculture, thereby gaining renewed economic value. This suggests that modifying aged vessels represents a highly promising and practical approach for the future development of fish farming vessels.

Based on the above motivation, this study focuses on a novel approach for converting aged bulk carrier into fish farming vessel. While retaining the bow and stern structures of the original bulk carrier, the side shell plating is largely replaced with aquaculture nets. Meanwhile, a transverse bulkhead is preserved amidships to create two large, fully open aquaculture tanks for the modified fish farming vessel. The use of permeable nets enables free water exchange while optimizing the vessel's seakeeping performance, which is the essential factor for the safe and stable operation of offshore aquaculture vessels. Previous experimental studies compared the seakeeping and motion responses of the modified and original vessels, demonstrating that the modification significantly reduced roll and heave responses [8]. However, given the high cost of physical testing, it is necessary to develop an efficient and reliable numerical method for further seakeeping performance evaluation of the modified vessel.

Seakeeping performance is crucial for the operational stability and safety of offshore structures [9, 10], and numerical simulation studies on the seakeeping of fish farming vessels have also seen notable development in recent years. For the offshore structures equipped with large-area aquaculture nets, similar to fully permeable fish farming vessel, the interaction between wave and floating structure has been well studied [11, 12], and the current key focus of hydrodynamic numerical simulation lies in the accurate modeling of the nets. The two main approaches used for simulating nets are the screen model [13, 14] and the Morison model [15-17]. In a hydrodynamic study of a semi-submersible fish farming platform, Bai et al. [18] employed the boundary element method (BEM) to compute the hydrodynamic coefficients of the semi-submerged structure. Meanwhile, the screen model was used to estimate the viscous loads acting on the net structure. By combining these two approaches, the frequency-domain hydrodynamic coefficients of the platform were obtained and subsequently applied in time-domain simulations to evaluate the platform's motions under both regular and irregular wave conditions. Li et al. [19] conducted a hydrodynamic study on the Havfarm fish farming vessel, in which each conical net structure was divided into five horizontal planes. Morison ring models was then established on each plane to approximate the drag forces acting on the net, while the deformation of the net was neglected. Chen et al. [20] studied a fish farming vessel similar to Havfarm. The net structures were also modeled as rigid. The arrangement of Morison elements is like a net and follows the assumption of uniform solidity to ensure the validity of the simulation. The same numerical approaches have also been widely applied to the seakeeping performance analysis of semi-submersible fish farm (SOFF) cages [21-23], which share similarities with fully permeable fish farming vessels. However, both models have certain limitations. The Morison model demands a large number of elements to accurately represent the net structure, resulting in significantly higher computational costs. The screen model requires relatively fewer computational resources but involves a more complex implementation process [24]. Moreover, in both approaches, the net structures are modeled separately from the main hull, which limits the ability to capture the hydrodynamic interactions between the nets and the vessel. Recent studies have also applied deep learning techniques to predict the

motion responses of floating ocean structures [25]. However, such approaches have not yet been extended to net-integrated structures. Therefore, a numerical approach that is both efficient and capable of accounting for the coupled hydrodynamics of the net structures and the hull is needed.

To address this need, this study adopts the dipole panel method to model the nets in the frequency-domain hydrodynamic analysis of the fish farming vessel. In this approach, the nets are idealized as porous boundaries characterized by a discharge coefficient, integrating porous media theory with potential flow theory within the boundary element method [22, 26, 27]. This modeling strategy enhances computational efficiency and allows the net structures, represented by dipole panels, to be incorporated into both diffraction and radiation analyses. It also facilitates the investigation of the hydrodynamic interaction between the hull and net, which is not accounted in both screen model and Morison model. This method has previously been applied successfully to assess the seakeeping performance of semi-open fish farming vessel in previous study [28]. The porous media theory has seen increasing application in the numerical modeling of nets for offshore aquaculture structures [29, 30]. Tian et al. [31] investigated the hydrodynamic performance of an aquaculture system composed of a jacket platform and a net cage, where the net cage was simplified as a closed box composed of six planar nets. Each planar net was modeled as a porous medium based on its equivalent hydrodynamic resistance. Liu et al. [32] employed a porous media model to represent the nets in the resistance prediction of a self-propelled fish farming vessel, and found that the shielding effect of the nets could reduce the overall resistance during navigation.

In summary, this study establishes a BEM model for a novel fish farming vessel by combining porous media theory with potential flow theory to investigate its seakeeping performance. The vessel hull is represented using panel elements, while the net structures are modeled using dipole elements. The numerical model is used to examine the effects of net solidity, wave slope and the presence of nets on the vessel's seakeeping behavior. Finally, the numerical results are compared with experimental data from free decay, regular waves, and white noise waves tests in the wave basin at Shenzhen International Graduate School of Tsinghua University to validate the accuracy of the proposed numerical model. The present study focuses on the frequency-domain analysis of the seakeeping performance of the novel fish farming vessel, while future work will build on this by combining developed methods to further investigate the vessel's dynamic motion response and sailing performance through numerical simulations [33-36].

This paper is organized as follows. Section 2 introduces the vessel concept and give a detailed explanation of experimental setup including the experimental facilities, arrangement and test conditions. Section 3 describes the fundamental theories and configurations of numerical model. Section 4 presents a detailed discussion of the results. Sections 4.1 and 4.2 focus on the effects of parameter variations and the presence of net structures on the seakeeping performance based on numerical simulations. Section 4.3 compares the numerical and experimental results to assess the accuracy and reliability of the proposed numerical model. Finally, conclusions are drawn in Section 5.

2. The concept of fish farming vessel and experiments

2.1 Vessel description

The novel concept of fish farming vessel is derived from the conversion of an aged bulk carrier. By replacing the side shell plating of cargo hold with aquaculture nets and retaining a transverse bulkhead near the midship section, the resulting vessel features two open aquaculture tanks. The conversion cost is lower compared to new built offshore aquaculture structures. Additionally, the bow and stern (including propulsion system) of the vessel remain unchanged, enabling the vessel to actively evade adverse sea conditions. The dimension and mass parameters of the novel fish farming vessel are listed in Table 1.

Table 1 Dimension and mass parameters of the novel fish farming vessel

Parameter	Symbol	Unit	Value
Length overall	L	m	89.60
Breadth	B	m	15.80
Depth	D	m	8.50
Draft	T	m	6.00
Displacement	Δ	t	3272
Center of gravity above BL[1]	VCG	m	3.20
Center of gravity from AP[2]	LCG	m	37.37
Radius of roll gyration	K_{xx}	m	5.00
Radius of pitch gyration	K_{yy}	m	30.00
[1] Baseline			
[2] Aft perpendicular			

2.2 Facilities and arrangements

The model tests of novel fish farming vessel are conducted in the wave basin at Shenzhen International Graduate School of Tsinghua University. The basin has dimensions of 25 m in length, 8 m in width, and a water depth of 5 m. It is equipped with a wave maker that can generate regular waves with a maximum height of 0.75 m and random waves with a maximum significant wave height of 0.40 m. The wave maker and wave-absorbing devices are located at opposite ends of the basin along its length as shown in Figure 2.

Fig. 2 The wave basin at Shenzhen International Graduate School of Tsinghua University

Considering these parameters along with the vessel dimensions at prototype, the experiment adopts a Froude scaling of 1:40 (λ). The model of vessel without nets is shown in Figure 3 (c). Based on practical industrial applications, three aquaculture nets designs with different solidity ratios (σ) of 0.190, 0.138, and 0.108 were developed. However, for the model nets, strictly scaling the twine diameter and mesh size according to the scale λ would pose challenges in fabrication of nets and significantly alter the local flow field around the nets due to substantial changes in net parameters. Therefore, in this experiment, the overall netting area is scaled following the scale λ, while the twine diameter and mesh size are adjusted with a smaller scale to ensure that the solidity ratio remains consistent with the prototype. The selected model nets are illustrated in Figure 3 and their parameters are presented in Table 2.
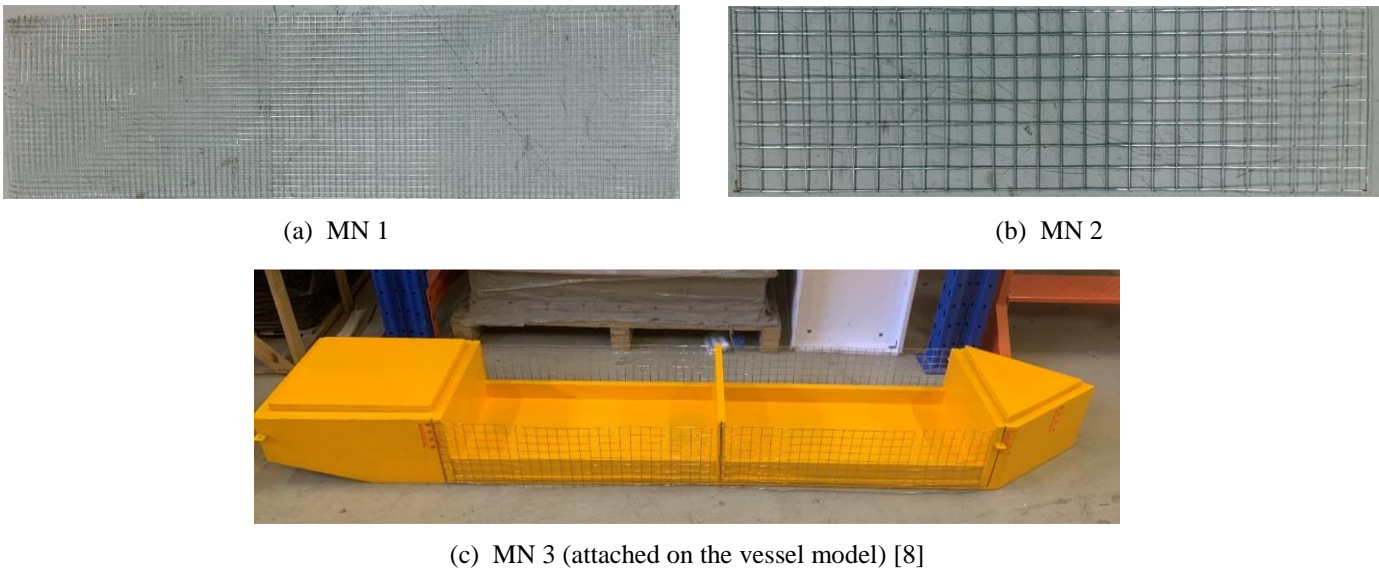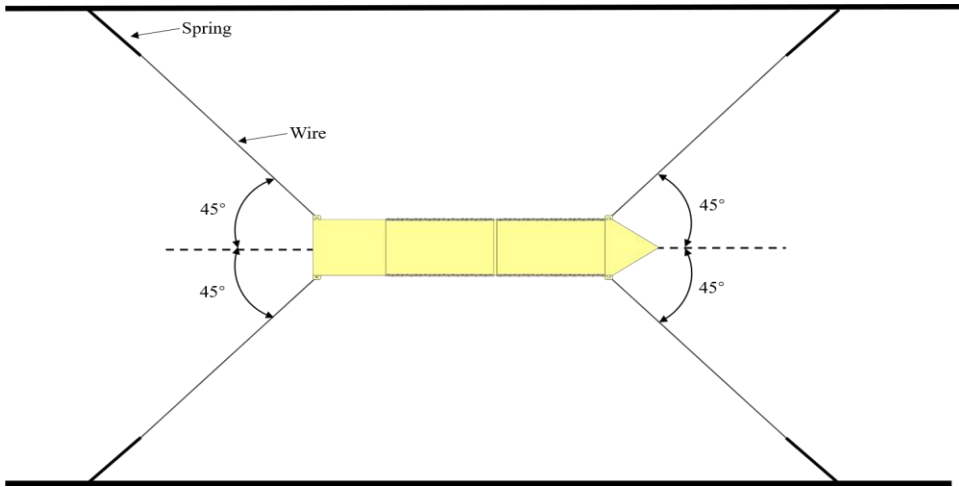
(a) MN 1

(b) MN 2

(c) MN 3 (attached on the vessel model) [8]

Fig. 3 The selected model nets

Table 2 Parameters of model nets

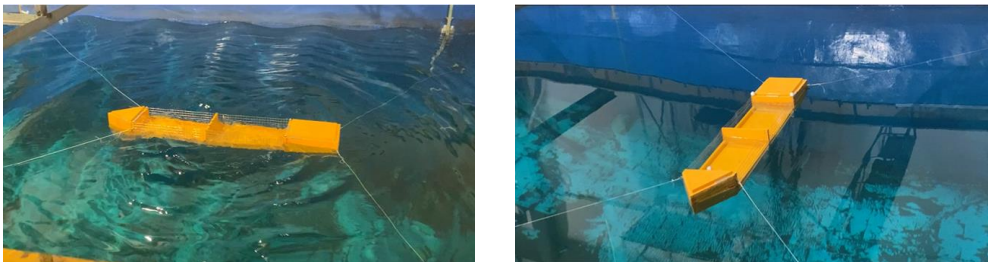| Nets	Solidity ratio σ (-)	Twine diameter (mm)	Twine length (mm)	Scale (-)
MN1	0.190	0.6	4.2	4.2
MN2	0.139	1.8	25	1.4
MN3	0.108	1.4	25	1.8

(a) Layout of the mooring system

(b) Head sea

(c) Beam sea

Fig. 4 The arrangement of vessel model and mooring system [8]

The instrumentation for measurement includes motion capture system and wave gauges. The motion capture system tracks the six-degree-of-freedom (6-DOF) motions of the vessel model in each test by recording the movement of markers attached to the model using cameras. The sampling frequency is set to 80 Hz. Meanwhile, the wave gauges record the wave elevation time history during each test, with a sampling frequency of 100 Hz.

For the arrangement of experimental facilities, the vessel model is positioned 8 m from the wave maker and centrally aligned in the basin's width direction. The mooring design of the vessel model is shown in Figure 4 (a). The wave attack angles considered were head seas and beam seas, with the vessel bow oriented perpendicular and parallel to the wave maker, respectively, as shown in Figure 4. Its primary purpose is to restrict the model's lateral movement while minimizing its impact on the model's first-order motions. Wave gauges are positioned between the wave maker and the vessel model, ensuring a 3 m separation from the model to minimize the influence of radiated waves from the model's motion on measurement of wave elevation. Four cameras of the motion capture system are arranged along the length of the wave basin, with their lenses adjusted to ensure full visibility of the markers on the model.

2.3 Test conditions

The free decay tests were conducted firstly to determine the natural periods of the vessel model in heave, roll, and pitch motions.

Table 3 Parameters of regular wave conditions at prototype scale

Wave attack angle	Condition	Wave height H (m)	Period T (s)
Head sea	EC1	1	5.69
	EC2	1	6.32
	EC3	2.4	6.96
	EC4	2.4	8.85
	EC5	2.4	9.49
	EC6	2.4	10.12
	EC7	1.2	11.38
	EC8	1.2	13.28
	EC9	1.2	14.55
	EC10	2.4	17.08
	EC11	2.4	18.97
Beam sea	EC12	1	4.93
	EC13	1	6.32
	EC14	2.4	8.85
	EC15	2.4	10.12
	EC16	2.4	11.38
	EC17	2.4	13.28
	EC18	2.4	13.91
	EC19	2.4	14.55
	EC20	2.4	17.71

Then, a numerical hydrodynamic model of the fish farming vessel was used to compute the RAOs for the vessel in 6-DOF motions before the main tests in wave basin. Based on the numerical results, the frequency range where significant variations occur in RAOs was selected to design the regular wave tests. The

corresponding wave heights and periods of regular wave test conditions at prototype scale are presented in Table 3. The wave height at prototype height was set to 2.4 m. However, during the experiments, wave-overtopping was observed under certain conditions, which could introduce nonlinear effects and compromise the accuracy of the measurements. To address this issue, the wave height was reduced for several conditions, including EC1, EC2, EC7–EC9, as well as EC12 and EC13.

Furthermore, white noise waves test was carried out to experimentally determine the RAO of the vessel model, which was compared with the numerical results for verification. The applied white noise waves have a significant wave height H_s of 2 m and cover a frequency range of 0.30 rad/s to 1.00 rad/s. Tests were conducted under both beam sea and head sea conditions.

Prior to the tests in wave basin, calibration of regular waves and white noise waves was performed to ensure that the actual wave generation by the wave maker aligned with the intended wave conditions. Additionally, tests were conducted under the same wave conditions with the vessel model fitted with three different types of nets.

3. Theory and numerical model

3.1 Basic computational theory

The engineering specifications of the novel fish farming vessel is described in Section 2.1. It is evident that the hydrodynamic characteristics of the vessel's hull and the aquaculture nets are different. Therefore, different boundary conditions are applied to the hull surface and the nets in the hydrodynamic solution.
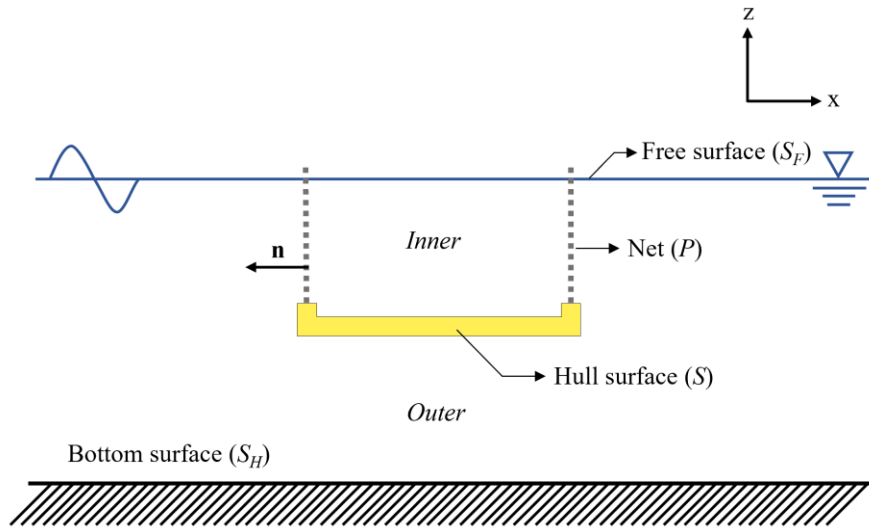
Fig. 5 Definition of boundary surface of the floating structure with porous part

The three-dimensional coordinate system $Oxyz$ is defined as shown in Figure 5, where the Oz axis is directed upward and Oxy plane coincides with the undistributed free surface. The vessel shown in the figure represent a cross-section of the aquaculture tank, consisting of the hull surface (S) and nets (P). Deep water is assumed, Additionally, assuming the fluid is incompressible and inviscid, and the flow is irrotational, a velocity potential Φ exists. Furthermore, the velocity potential can be written as following version based on the assumption of steady-state conditions:

$$\Phi(x, y, z, t) = \text{Re}\big[\phi(x, y, z)e^{-i\omega t}\big] \tag{1}$$

where ω denotes the angular frequency of oscillation, and t is time. Within the assumptions of potential flow theory, the spatial velocity potential ϕ can be decomposed in to superposition of multiple velocity potentials, expressed as following:

$$\phi(\mathbf{x}) = \phi_0(\mathbf{x}) + \phi_7(\mathbf{x}) - i\omega \sum_{j=1}^{6} \xi_j \phi_j(\mathbf{x}) \tag{2}$$

where ϕ_0 is the incident wave potential, ϕ_7 is the diffraction potential and ϕ_j (j=1, 2, ..., 6) are the radiation potential. $\mathbf{x}$ is (x, y, z) and denotes the flow-field point. ξ_j with j=1, 2, ..., 6 denotes the amplitudes in the jth motion mode. The diffraction-radiation potentials ϕ_j (j=1, 2, ..., 7) should satisfy the conditions, including Laplace equation in the fluid domain, the impermeability condition at the sea bead, the linear free surface condition and the Sommerfeld condition at the far field, listed as following:

$$\begin{cases} \nabla^2 \phi_j = 0 & \mathbf{x} \in D \\ \dfrac{\partial \phi_j}{\partial z} = 0 & \mathbf{x} \in S_H \\ -k_0 \phi_j + \dfrac{\partial \phi_j}{\partial z} = 0 & \mathbf{x} \in S_F \\ \sqrt{r} \left(\dfrac{\phi_j}{r} - ik_0 \phi_j \right) = 0 & r \to +\infty \end{cases} \tag{3}$$

where k_0 is the wave number. Considering that the designated operating areas of the vessel are located in deep-water regions, where the water depth is significantly greater than both the wavelength and the vessel draft, the following theoretical analysis is conducted under the deep-water assumption. Accordingly, the wave number k_0 satisfies the dispersion relation in deep water:

$$k_0 = \omega^2/g \tag{4}$$

The boundary condition on the impermeable hull surface is expressed as:

$$\frac{\partial \phi_j}{\partial n} = n_j \qquad \mathbf{x} \in S \tag{5}$$

For the net surface, it can be regarded as infinitely thin porous medium with numerous fine pores, allowing the application of Darcy's law. This implies that the normal relative velocity remains continuous and is linearly proportional to the pressure drop across the porous surface:

$$\frac{\partial \phi_j^{out}}{\partial n} = \frac{\partial \phi_j^{in}}{\partial n} = n_j - i\frac{bk_0}{2\pi}(\phi_j^{out} - \phi_j^{in}) \qquad \mathbf{x} \in P \tag{6}$$

where the subscripts ^{out} and ^{in} denote the outer and inner sides of the porous surface in Figure 6, respectively. The discharge coefficient b determines the permeability of the net, being impermeable when b is 0 and completely transparent when b becomes infinitely large. Additionally, n_j in Equations (5) and (6) is expressed as:

$$n_j = \begin{cases} n_j & j = 1, 2, 3 \\ (\mathbf{r} \times \mathbf{n})_{j-3} & j = 4, 5, 6 \\ -\mathbf{n} \cdot \nabla \phi_0 & j = 7 \end{cases} \tag{7}$$

The boundary value problem given by Equations (3), (5) and (6) can be solved by using the boundary element method with the free-surface Green function as the fundamental solution. In the present study, we adopted the direct dipole distribution on the net surface [37] rather than the multi-domain boundary element method requiring the identification of internal and external subdomains [38, 39]. In the present problem, Green function is written as [40, 41]:

$$G(\mathbf{x}, \mathbf{x}') = -\frac{1}{r} - \frac{1}{r'} + G^F \tag{8}$$

where $\mathbf{x}'$, expressed as (x', y', z'), denotes the singularity point, and $\mathbf{x}''$, expressed as $(x', y', -z'')$, represents the symmetrical point of $\mathbf{x}'$ with respect to the free surface (where z is 0). The variable r (or r', respectively) refers to the distance between $\mathbf{x}$ and $\mathbf{x}'$ (or $\mathbf{x}''$, respectively), defined as:

$$\begin{cases} r = \sqrt{(x-x')^2 + (y-y')^2 + (z-z')^2} \\ r' = \sqrt{(x-x')^2 + (y-y')^2 + (z+z')^2} \end{cases} \tag{9}$$

G^F denotes the free-surface term in the Green function, expressed as:

$$G^F = -\int_0^\infty \frac{2k_0}{k-k_0} e^{k(z+z')} J_0(kR) \, dk \tag{10}$$

where R denotes the distance between the singularity point and the field point:

$$R = \sqrt{(x-x')^2 + (y-y')^2} \tag{11}$$

Thus, the boundary integral equation for the hull surface can be expressed as:

$$2\pi\phi_j(\mathbf{x}) + \iint_S \phi_j(\mathbf{x}') \frac{\partial G(\mathbf{x},\mathbf{x}')}{\partial n_{\mathbf{x}'}} dS + \iint_P \psi_j(\mathbf{x}') \frac{\partial G(\mathbf{x},\mathbf{x}')}{\partial n_{\mathbf{x}'}} dS$$
$$= \iint_S \frac{\partial \phi_j(\mathbf{x}\,')}{\partial n_{\mathbf{x}'}} G(\mathbf{x},\mathbf{x}\,') dS \qquad \mathbf{x} \in S \tag{12}$$

For the nets, the boundary integral equation constructed on the porous surface is:

$$\iint_S \phi_j(\mathbf{x}') \frac{\partial^2 G(\mathbf{x},\mathbf{x}')}{\partial n_{\mathbf{x}} \partial n_{\mathbf{x}'}} dS + \iint_P \psi_j(\mathbf{x}') \frac{\partial^2 G(\mathbf{x},\mathbf{x}')}{\partial n_{\mathbf{x}} \partial n_{\mathbf{x}'}} dS$$
$$= \iint_S \frac{\partial \phi_j(\mathbf{x}')}{\partial n_{\mathbf{x}'}} \frac{\partial G(\mathbf{x},\mathbf{x}')}{\partial n_{\mathbf{x}}} dS - 4\pi \frac{\partial \phi_j(\mathbf{x})}{\partial n_{\mathbf{x}}} \qquad \mathbf{x} \in P \tag{13}$$

where ψ is defined as the difference between the outer and inner potentials of nets ($\phi_j^{out} - \phi_j^{in}$). The following equation is supplemented to ensure that the solution is free of irregular frequencies [42]:

$$\iint_S \phi_j(\mathbf{x}') \frac{\partial G(\mathbf{x},\mathbf{x}')}{\partial n_{\mathbf{x}'}} dS + \iint_P \psi_j(\mathbf{x}') \frac{\partial G(\mathbf{x},\mathbf{x}')}{\partial n_{\mathbf{x}'}} dS$$
$$= \iint_S \frac{\partial \phi_j(\mathbf{x}')}{\partial n_{\mathbf{x}'}} G(\mathbf{x},\mathbf{x}') dS \qquad \mathbf{x} \in S_W \tag{14}$$

The diffraction-radiation potentials ϕ_j ($j = 1, 2, ..., 7$) of the flow field can be solved using Equations (12) and (13). Subsequently, the hydrodynamic forces acting on the surface of the aquaculture vessel and its hydrodynamic coefficients can be obtained through the following integral expressions:

$$\begin{cases} \mathbf{F}^{ex} = -i\omega\rho \left[\iint_S (\phi_0 + \phi_7)\mathbf{n} dS + \iint_P \psi_7 \mathbf{n} dS \right] \\ i\omega A_{ij} - B_{ij} = -i\omega\rho \left(\iint_S \phi_j n_i dS + \iint_P \psi_j n_i dS \right) \quad i,j = 1,2,\ldots,6 \end{cases} \tag{15}$$

where A is added mass and B denotes the radiation damping.

The numerical simulations in this study were performed using Hydrostar [43], which has been extensively validated in various engineering applications [44-46]. The use of dipole distribution on the rigid perforated net requires the calculation of second derivatives of the Green function which exhibits hypersingular behaviours [47].

3.2 Numerical model setup

The numerical model of the novel fish farming vessel was constructed by panel elements with the combined source and dipole distribution on the net of negligible thickness. As shown in Figure 6 (a), the numerical model of the novel fish farming vessel consists of panel elements and dipole elements. Specifically, 3208 panel elements are used to represent the impermeable hull surface, while 560 dipole elements with discharge coefficient b are employed to simulate the net structure of the vessel. The discharge coefficient b is employed to reflect the pressure drop effect of the metal net to the fluid. Thus, it can be applied to represent net with different solidities. A discharge coefficient b of zero corresponds to an impermeable surface element (a solidity of 1), while an infinitely large discharge coefficient represents a fully permeable element (a solidity of 0). Furthermore, the empirical relationship between the discharge coefficient and the solidity of net can be defined as follows [48]:

$$b = \frac{\left(\frac{17.8}{\varepsilon} + 143.2\right)(1 - \sigma)^2}{2.06 - 1.06\sigma} \tag{16}$$

where ε denotes the wave slope, defined as the product of the wave amplitude ζ and the wave number k.

(a) With nets   (b) Without nets
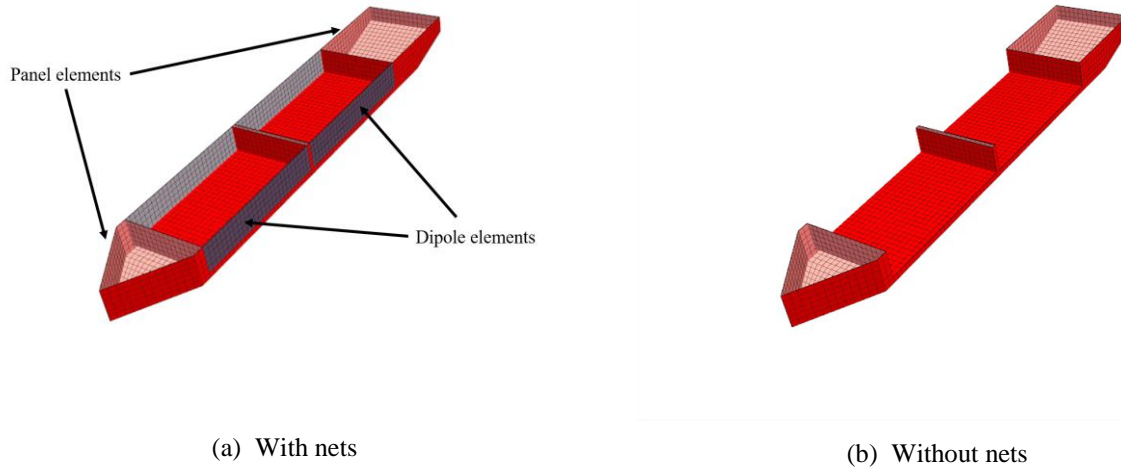
Fig. 6 The numerical model of the fish farming vessel

In addition, the numerical model that includes only the hull without nets was established, as shown in Figure 6 (b). This model is used to demonstrate the influence of the nets on calculation of hydrodynamic results.

4.   Results and discussions

Based on the numerical model proposed in the former section, this section performs three-dimensional diffraction and radiation analyses under the assumption of infinite water depth. The hydrodynamic responses, including RAOs, added mass, radiation damping, wave excitation forces and moments, are computed. As the discharge coefficient of dipole elements is related with the solidity of net and wave slope, Section 4.1 investigates the influence of net solidity and wave slope on the RAO predictions, which are related to the discharge coefficient. Moreover, the frequency-dependent hydrodynamic results were adopted in Section 4.1.2 as the final numerical representation of the vessel's seakeeping performance and are used throughout the following comparisons and evaluations. Then, Section 4.2 compares the RAOs of the vessel with and without the nets. The impact of the net on seakeeping performance is further evaluated by analysing changes in the hydrodynamic coefficients. Finally, Section 4.3 compares the numerical results with physical model tests. The computed natural periods in heave, roll, and pitch motions are compared with free-decay tests, while RAOs are validated against regular and white-noise waves experiments. Physical observations are discussed to

interpret the discrepancies between numerical and experimental results. The frequency interval for all numerical results was set to 0.02 rad/s, which is independent of the density of the dots shown along the dash-dot lines.

4.1 Effects of parameters related to the discharge coefficient

4.1.1   Effects of solidity ratio

As shown in Equation (16) from Section 3.2, changing the nets with different solidity modifies the discharge coefficient of the dipole elements in the numerical model. Therefore, this section investigates the effect of varying net solidity on the seakeeping performance of the vessel.

A total of five numerical models were established, and the solidity ratio of nets and corresponding discharge coefficients are listed in Table 4. NM1 to NM3 correspond to the net MN1 to MN3 listed in Table 2, which were used in the experiments. Since the solidity ratios of these three nets are relatively close, two additional models, NM4 and NM5, were introduced to examine the impact of larger variations in solidity ratio on the results. However, it should be noted that in practical engineering applications, the net solidity typically remains below 20%. Meanwhile, as indicated by Equation (16), the wave slope ε varies with frequency in the RAO calculation, which in turn leads to variations in the discharge coefficients. In this subsection, the effect of wave slope variation is not considered, and a constant value of 0.040 is used.

Table 4 Solidity ratios and discharge coefficients of different numerical models

Numerical model ID	Solidity ratio σ	Discharge coefficient b
NM1	0.190	207.639
NM2	0.139	228.382
NM3	0.108	240.558
NM4	0.400	129.433
NM5	0.600	66.089

The analysis considers both head sea and beam sea conditions for surge, heave and pitch motions, while sway, roll, and yaw motions are examined only under beam sea condition. The RAOs of each motion are illustrated in Figures 7-10. It can be observed that the motion responses of NM1 to NM3, which correspond to the actual nets used in the experiments, are nearly identical, showing no significant differences. In contrast, the results for NM4 and NM5, which represent models with significantly different solidity ratios, deviate considerably from models NM1 to NM3. Specifically, as the net solidity increases, the surge and pitch motions under beam seas, along with the heave motion under head seas, exhibit decreased peak values near 0.40 rad/s and 0.68 rad/s. Under beam wave conditions, the heave motion exhibits less significant fluctuation around 0.40 rad/s. This is attributed to the increased damping effect during the vessel's motion as the net solidity increases, resulting in decreased motion amplitudes and fluctuation of RAO. In addition, under beam wave conditions, the roll motion shows a decreasing peak near 0.49 rad/s as the net solidity increases. This observation is also attributed to the increased damping, which enhance the resistance to roll motion and consequently reduces the corresponding motion response.

It should be noted that changes in net solidity have little influence on the natural frequencies of the aquaculture vessel. The natural period for heave motion is close to 0.40 rad/s, for roll motion around 0.49 rad/s, and for pitch motion approximately 0.69 rad/s. This indicates that the influence of net solidity on the vessel's RAOs is mainly concentrated near these natural frequencies. And the RAO values near these frequencies generally decrease as the net solidity increases. Moreover, the effect of changes in solidity on the RAO becomes negligible when the net solidity changes within the range of metal nets applied in offshore aquaculture.
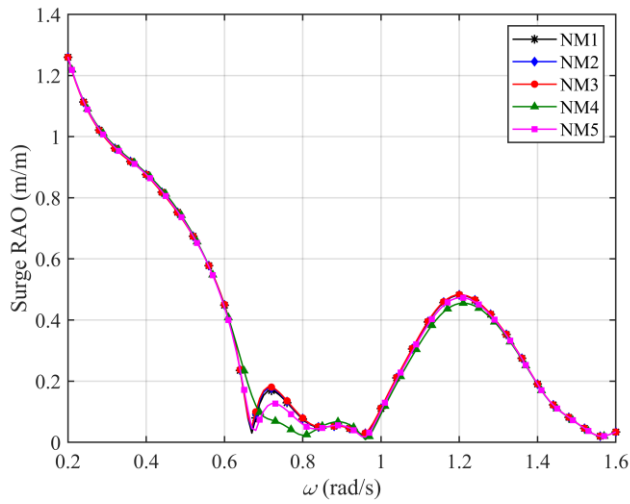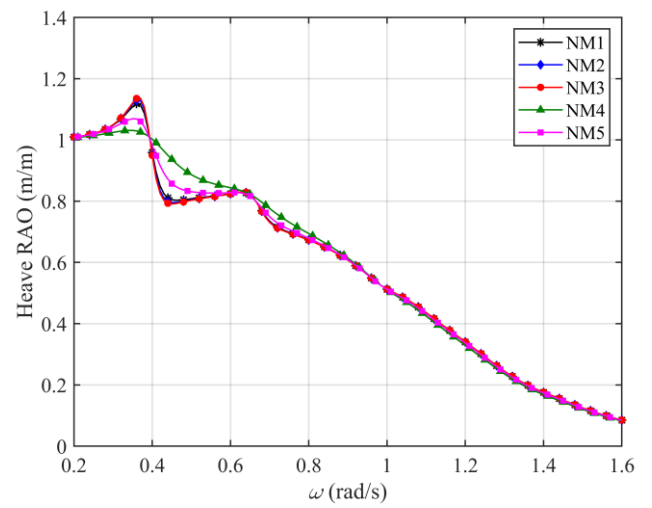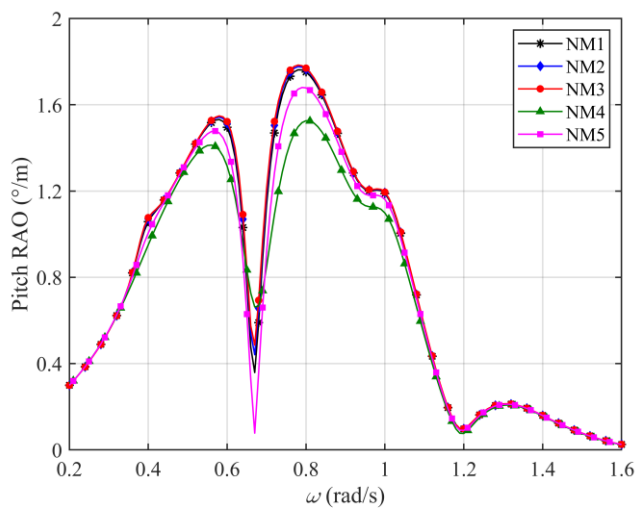
(a) Head sea
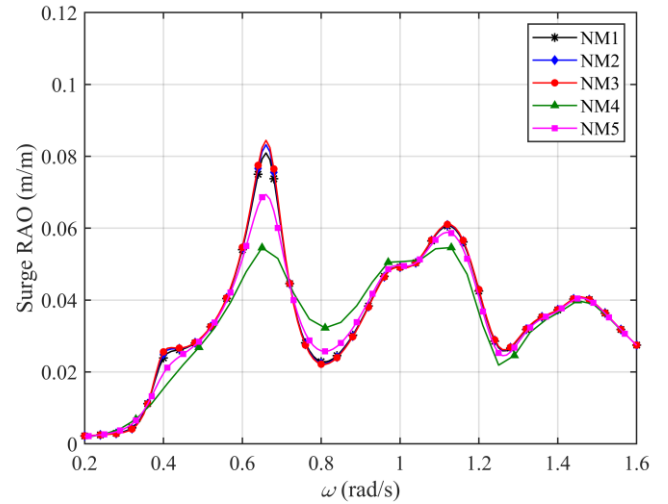
(b) Beam sea

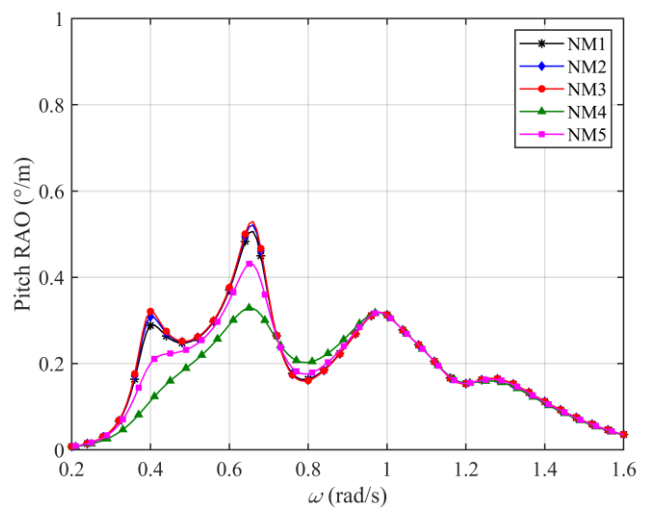**Fig. 7** The surge motion RAOs of vessels with different nets
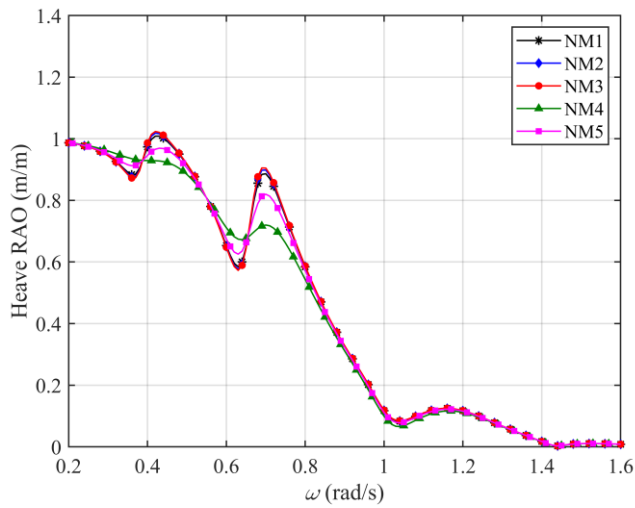
(a) Head sea

(b) Beam sea

Fig. 8 The heave motion RAOs of vessels with different nets

(a) Head sea

(b) Beam sea

Fig. 9 The pitch motion RAOs of vessels with different nets
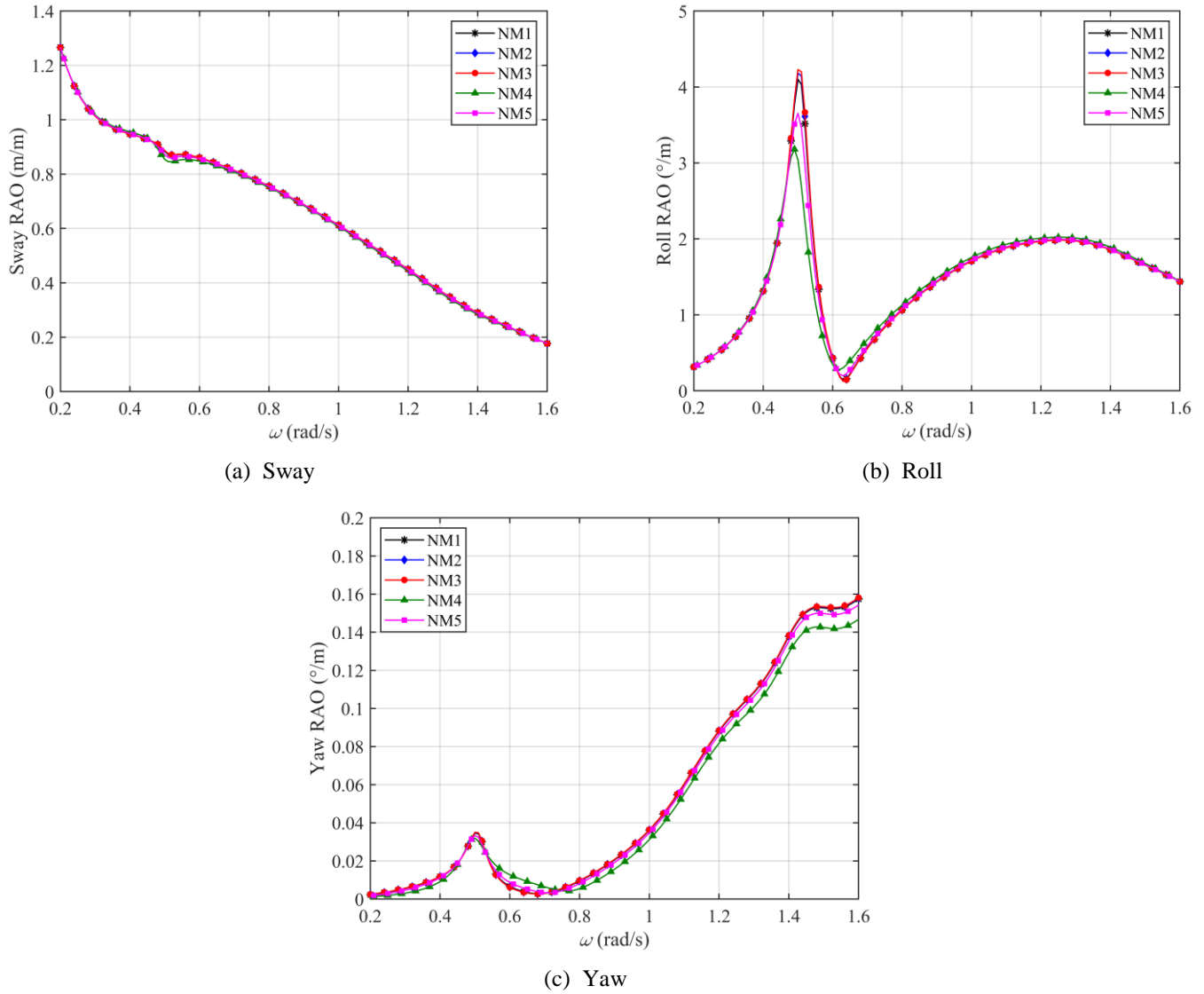
13

(a) Sway

(b) Roll

(c) Yaw

Fig. 10 The sway, roll and yaw motion RAOs of vessels with different nets under beam sea

4.1.2   Effects of wave slope

As shown in Equation (16), the discharge coefficient of the net is related to both the net's solidity and the wave slope of the incident waves. However, under the real marine operations involving random waves, the net properties remain fixed, while the wave slope continuously varies. Therefore, this subsection investigates the influence of wave slope on the seakeeping performance of the fish farming vessel using the numerical model.

The numerical model NM1 is selected as an example, with the net solidity set to 0.190. Numerical simulations are carried out over the frequency range of 0.2–1.6 rad/s, and the corresponding wave slope values ε and discharge coefficients b are listed in Table 5. Since the variations in RAOs are mainly concentrated in the range of 0.2–1 rad/s, six cases were selected within 0.2–1.2 rad/s at an interval of 0.2 rad/s for analysis. In addition, the cases all satisfy the linear wave assumption. It can be observed that variations in discharge coefficient ranging from 90 to 1600, which means the variation in wave slop leads to a significant change in the discharge coefficient.

The calculation of hydrodynamic parameters requires building corresponding numerical models for each discharge coefficient associated with different wave frequencies. From each model, the results at the frequency corresponding to the given discharge coefficient are selected and then complied to obtain the variation of the vessel's hydrodynamic parameters with frequency. Therefore, eight numerical models with fixed discharge

coefficients, as listed in Table 5, were established and simulations were carried out over the wave frequency range of 0.2-1.6 rad/s.

Table 5 Discharge coefficients and wave slope of different wave frequencies

Frequency (rad/s)	Wave slope ε	Discharge coefficient b
0.2	0.004	1591.59
0.4	0.016	438.81
0.6	0.037	207.64
0.8	0.065	146.87
1.0	0.100	112.19
1.2	0.150	93.36

Firstly, the resulting RAOs from each model illustrated in Figure 11-14 were compared to analyse the impact of a wide range of discharge coefficient variations (from 93.36 to 1591.59) on the simulated seakeeping performance of the vessel. For comparison purposes, the RAO results of the model without nets are also included in the figures. It can be observed that the motion of the fish farming vessel varies significantly with the discharge coefficient in the frequency range of 0.2-1.0 rad/s, while the motion at frequencies above 1.0 rad/s for different coefficients become identical. Among the six degrees of freedom, sway and yaw motions are relatively insensitive to changes in the discharge coefficient and their RAOs closely match those of the model without nets. In contrast, the RAOs of the other four motions show greater sensitivity to these variations. This observation indicates that sway and yaw motions are primarily driven by wave excitation acting on the hull under beam sea, while the influence of the net-induced forces is relatively limited. In addition, the RAO values near the natural frequencies of the motions increase with the discharge coefficient. This trend is observed near 0.40 rad/s for heave motion, around 0.48 rad/s for roll motion, and approximately 0.68 rad/s for pitch motion. Besides, as discussed in Section 3.2, when the discharge coefficient b approaches infinity, the net is considered fully permeable. The results show that the RAOs corresponding to discharge coefficient of 1591.59 are generally close to those of the model without nets for most motions, with the exception of roll. For roll motion, the RAO of the model without nets aligns more closely with the result obtained using a discharge coefficient of 207.64. This suggests that an excessively large b value may lead to an overestimation of the RAO of roll motion near the natural frequency.
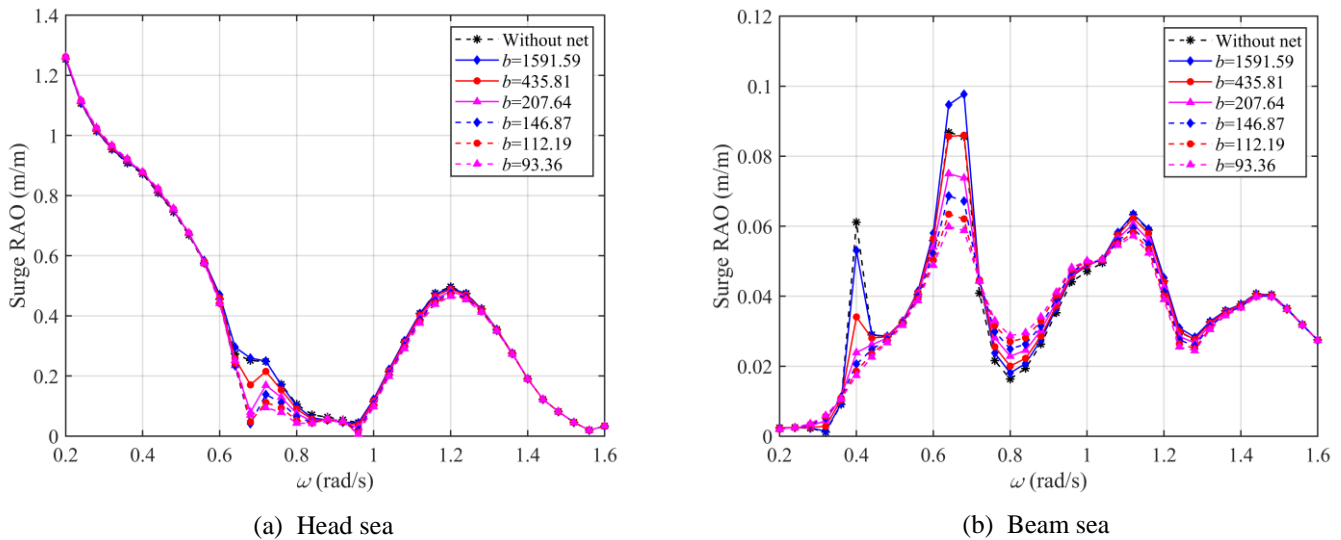
(a) Head sea   (b) Beam sea

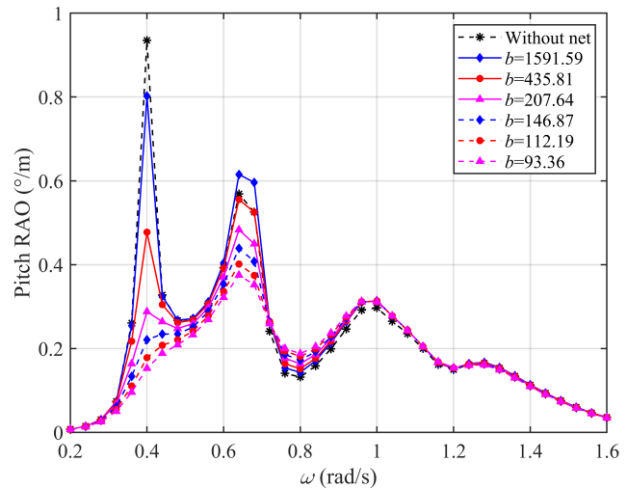**Fig. 11** The surge motion RAOs with different discharge coefficients
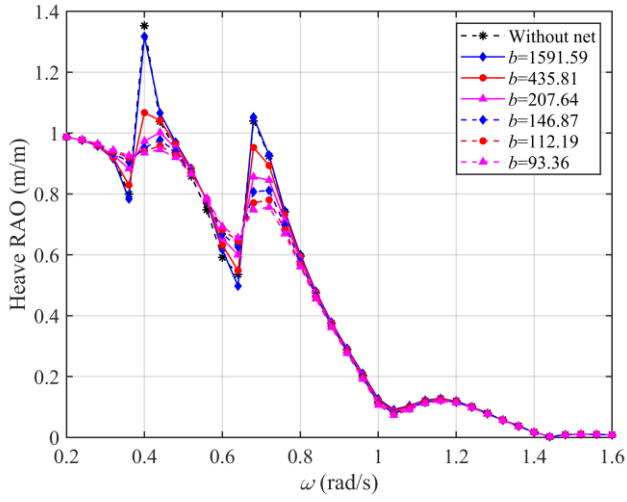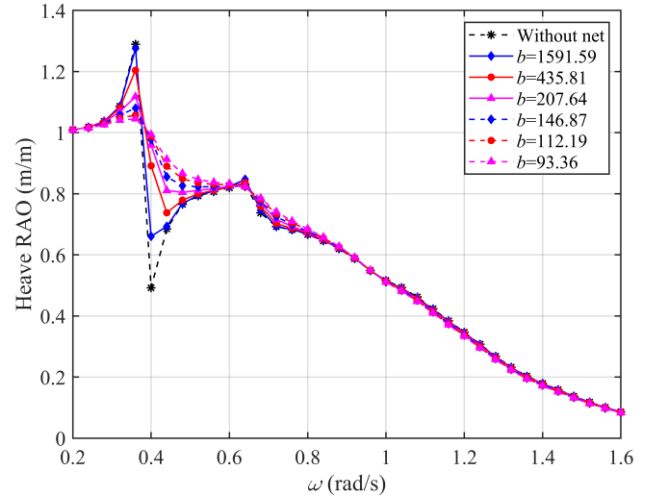
(a) Head sea

(b) Beam sea

Fig. 12 The heave motion RAOs with different discharge coefficients
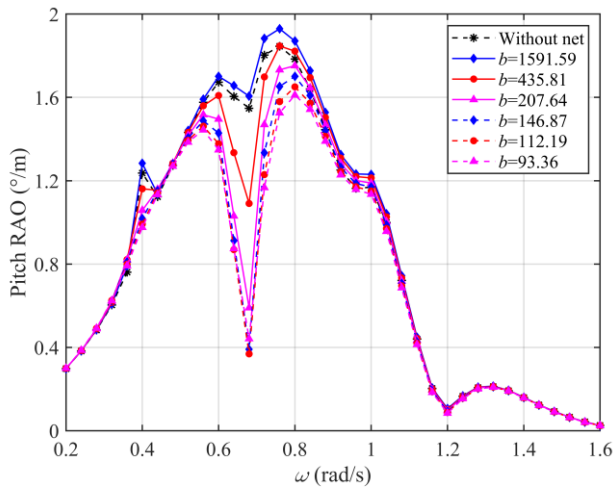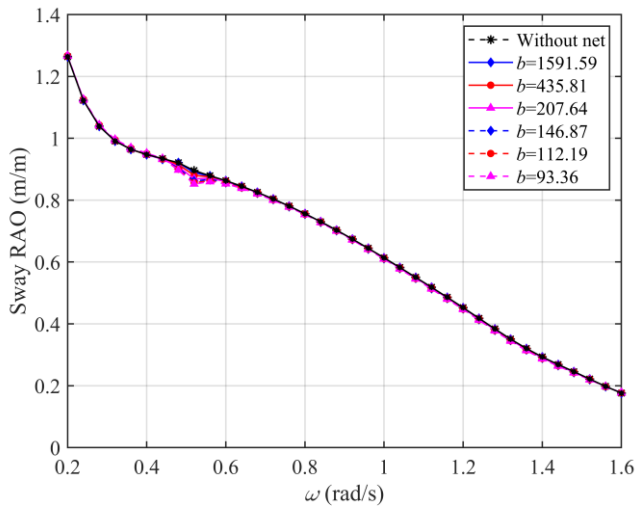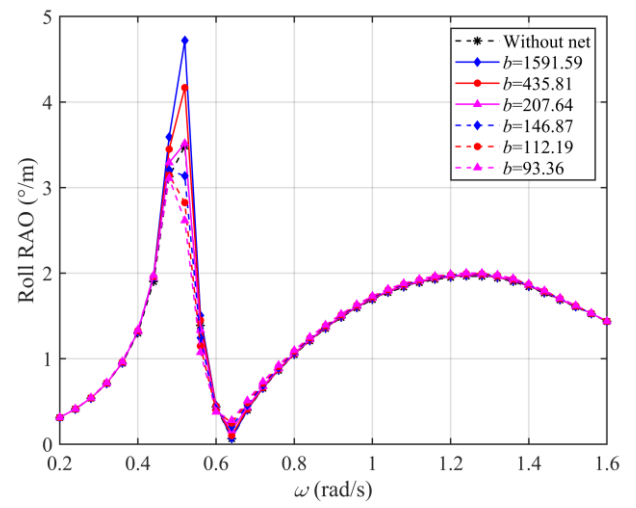

(a) Head sea

(b) Beam sea

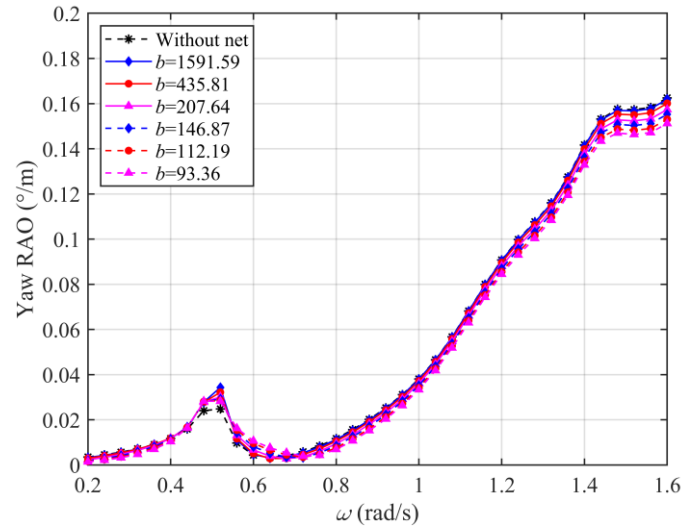**Fig. 13** The pitch motion RAOs with different discharge coefficients

Subsequently, data at selected frequencies are extracted from the models of different discharge coefficient to plot the RAO variation with respect to changes in the porosity effect coefficient driven by wave slope. To evaluate the influence of different calculation approaches on the results, a set of RAO results with a fixed discharge coefficient (b=146.87) is also included. Moreover, to facilitate the analysis of the differences in RAOs from each approach, the added mass, damping and wave excitation forces for surge, heave, and pitch motions are also presented. These results are shown in Figure 15-21.

(a) Sway

(b) Roll

(c) Yaw

Fig. 14 The sway, roll and yaw motion RAOs with different discharge coefficients under beam sea
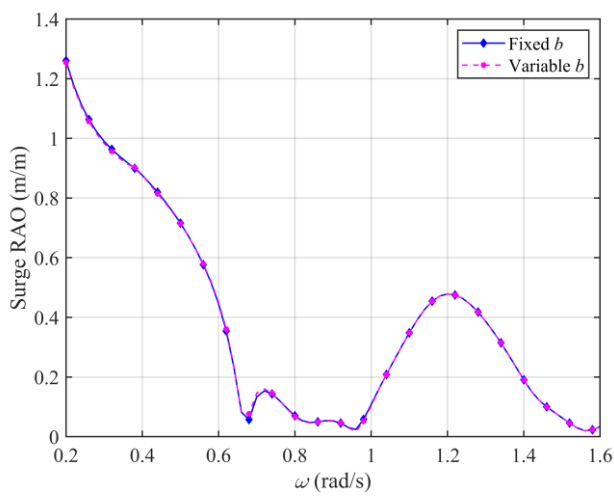
(a) Head sea
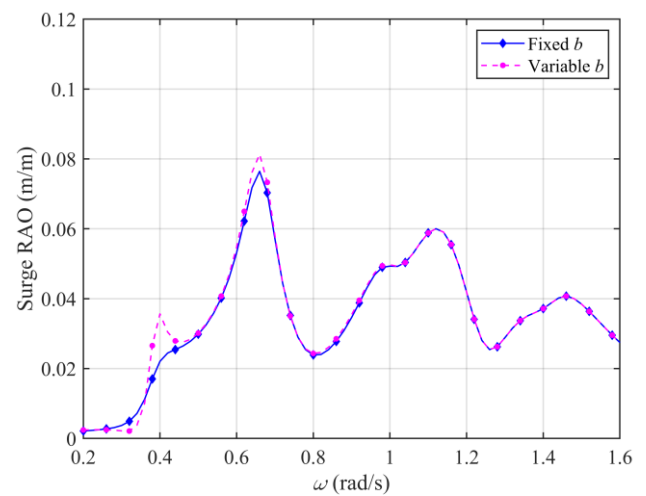
(b) Beam sea

Fig. 15 The surge motion RAOs with fixed and variable discharge coefficients

For the surge motion RAOs shown in Figure 15, it can be observed that under head sea, the results from both calculation methods are nearly identical. However, under beam sea, the results with variable porosity effect coefficients are slightly higher around 0.40 rad/s and 0.68 rad/s. By referring to the wave force and hydrodynamic coefficients presented in Figure 16, this increase is attributed to the lower added mass and radiation damping of the variable-coefficient case.

(a) Added mass

(b) Damping

(d) Wave force (head sea)

(d) Wave force (beam sea)
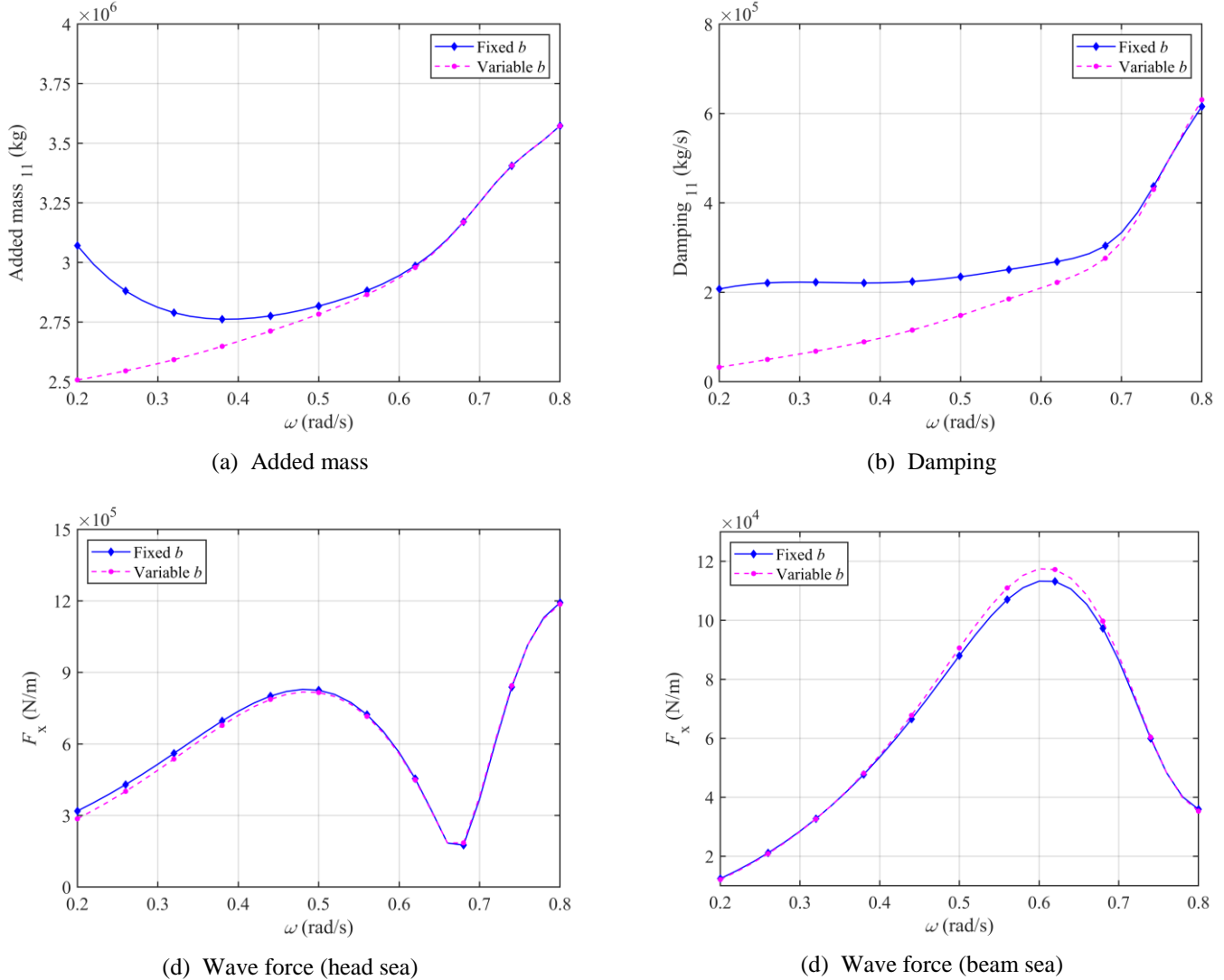
Fig. 16 The hydrodynamic coefficients and wave force of surge motion with fixed and variable discharge coefficients

Regarding the heave motion RAOs shown in Figure 17, it can be observed that the differences between the two results occur around 0.40 rad/s, and the variation trends differ under different wave attack angles. Under head sea, the RAO of variable discharge coefficient shows a higher peak before 0.40 rad/s and a deeper trough after 0.40 rad/s. In contrast, under beam wave conditions, the variable-coefficient result exhibits a lower trough before 0.40 rad/s and a higher peak after 0.40 rad/s. Based on the results illustrated in Figure 18, the main reason is attributed to the differences in wave forces under different wave attack angles. Under head sea, the maximum difference in wave force between the two calculation approaches occurs near 0.405 rad/s. At this frequency, the RAO of the variable-coefficient approach exceeds that of the fixed-coefficient case, and the difference reaches its largest value. A similar trend can be seen under beam sea, where the maximum difference occurs around 0.445 rad/s.

For the pitch motion, the difference between the two calculation approaches is mainly concentrated around 0.40 rad/s, where the result of the variable-coefficient model exhibits a distinct peak. Referring to the hydrodynamic coefficients presented in Figure 20, it is observed that the radiation damping of the variable-coefficient result is lower than that of the fixed-coefficient model at this frequency, which contributes to a

higher RAO. At the same time, the added mass in the variable-coefficient results increases gradually, which has a suppressing effect on the increase of RAO. As a result, a peak forms near 0.40 rad/s, followed by a decrease in RAO beyond this frequency due to the increasing added mass.
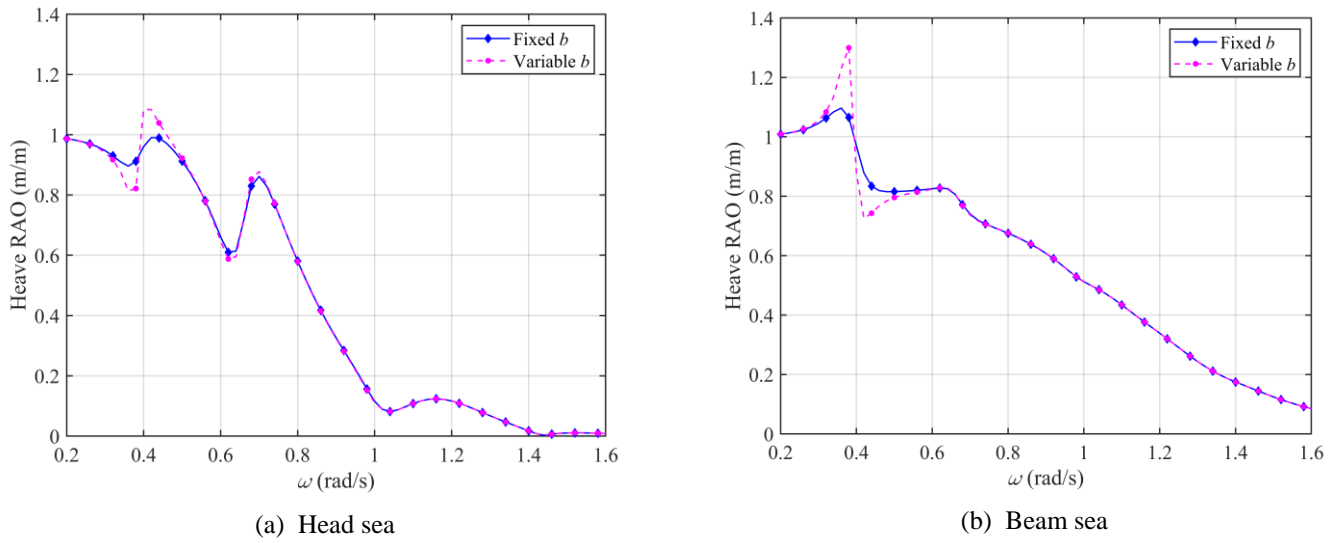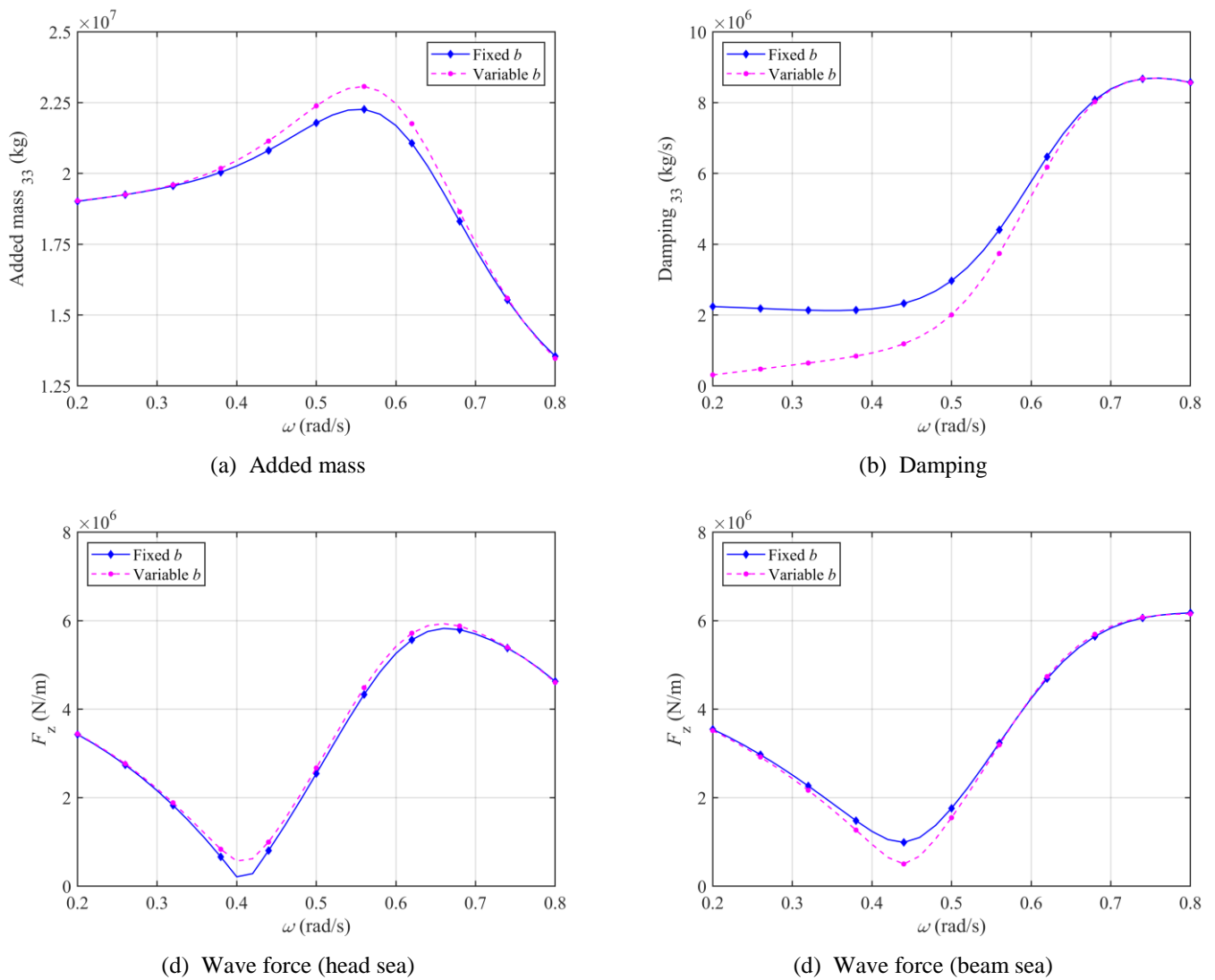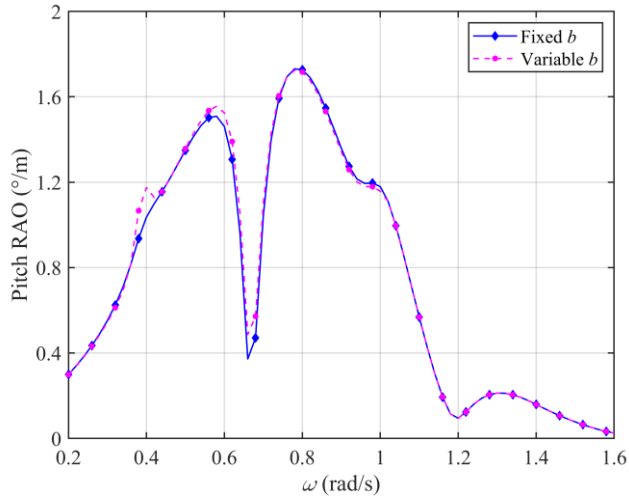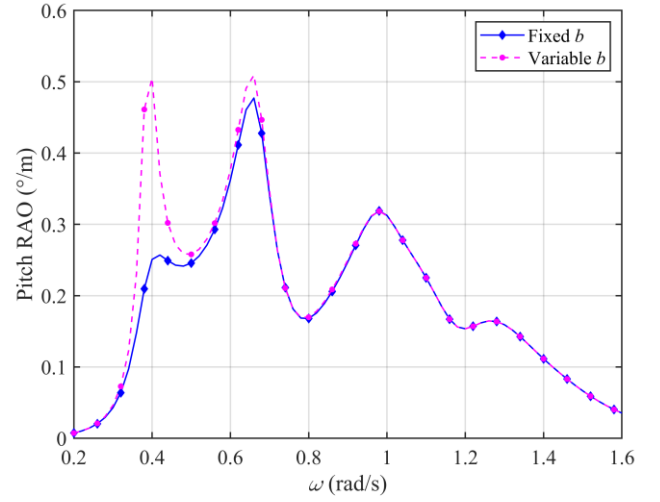

(a) Head sea

(b) Beam sea

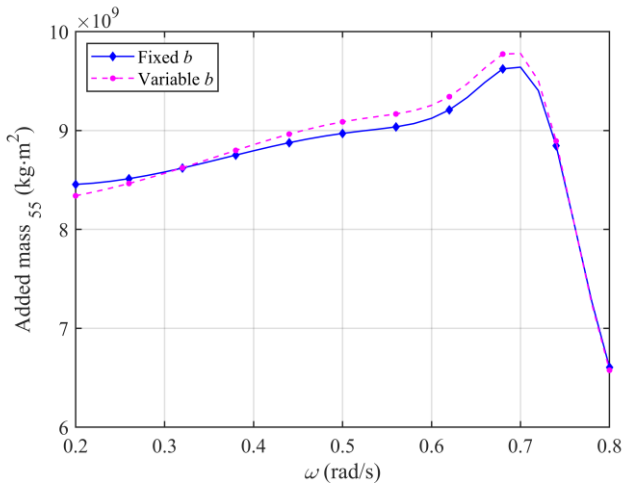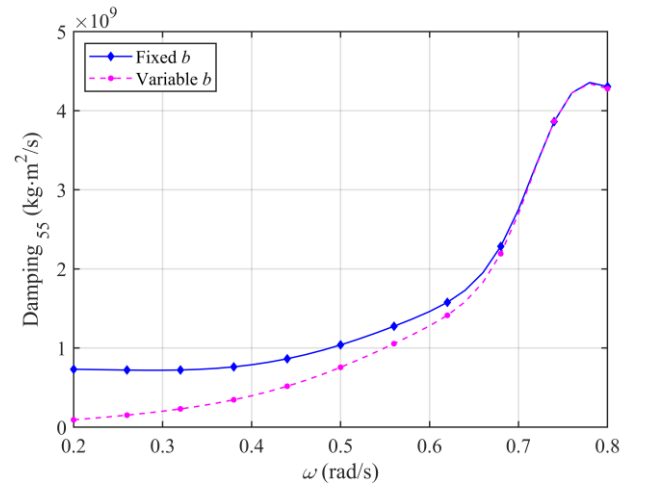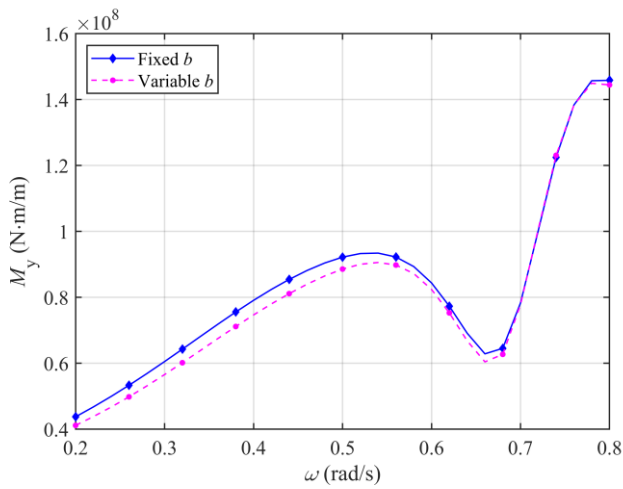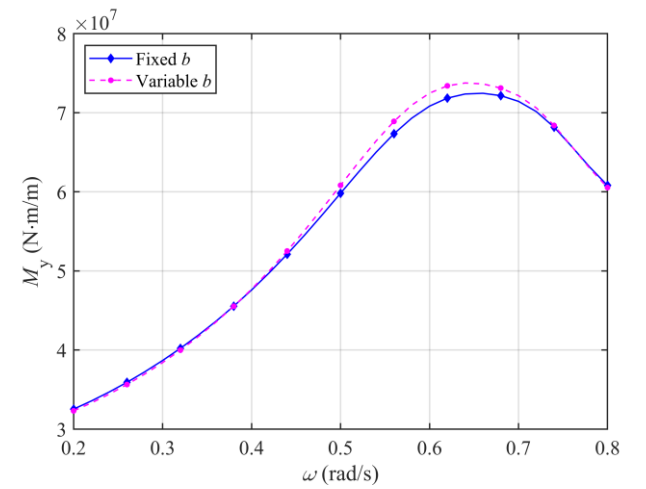**Fig. 17** The heave motion RAOs with fixed and variable discharge coefficients

(a) Added mass

(b) Damping

(d) Wave force (head sea)

(d) Wave force (beam sea)

Fig. 18 The hydrodynamic coefficients and wave force of heave motion with fixed and variable discharge coefficients

19

(a) Head sea

(b) Beam sea

Fig. 19 The pitch motion RAOs with fixed and variable discharge coefficients

(a) Added mass

(b) Damping

(d) Wave force (head sea)

(d) Wave force (beam sea)

Fig. 20 The hydrodynamic coefficients and wave force of pitch motion with fixed and variable discharge coefficients
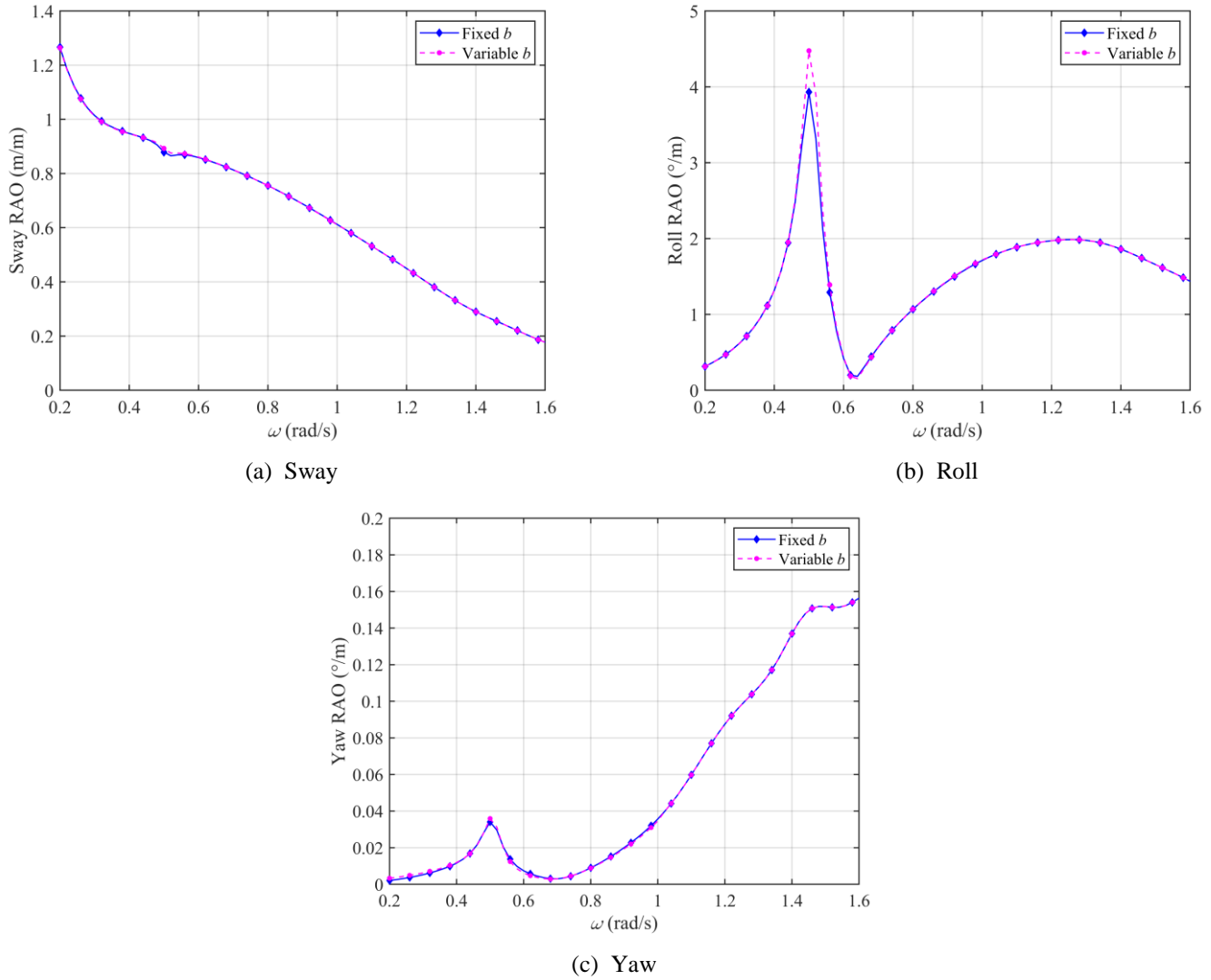
(a) Sway

(b) Roll

(c) Yaw

Fig. 21 The sway, roll and yaw motion RAOs with fixed and variable discharge coefficients

Finally, with the analysis of Figure 21 under beam sea, the results for sway and yaw motions show virtually no difference between the two calculation approaches. For roll motion, the RAO of the variable-coefficient case is slightly higher near 0.49 rad/s, while at other frequencies, the results closely match those of the fixed-parameter case.

In summary, it is observed that the RAOs calculated using the fixed-parameter approach tend to be slightly lower than those from the variable-parameter method near the vessel's natural frequencies at 0.40 rad/s, 0.49 rad/s, and 0.68 rad/s.

Therefore, it can be concluded that the variable-coefficient approach, which accounts for the variation of wave slope with frequency, provides a more accurate prediction of RAO behaviour near the natural frequencies.

4.2 Effects of nets

Based on the preceding discussion, it can be concluded that variations in net solidity within the practical range have a negligible impact on the seakeeping performance of the novel fish farming vessel in numerical simulations. In contrast, the variation of wave slope with frequency significantly affects the RAO prediction near the vessel's natural frequencies. Therefore, in this study, the seakeeping performance of the fish farming vessel is numerically represented by the hydrodynamic results of model NM1 considering wave slope variation, as presented in Section 4.1.2.

In this subsection, these results are compared with those of the model without nets to investigate the influence of the nets on the seakeeping performance of the novel fish farming vessel. Figures 22-29 illustrate the motion RAOs, hydrodynamic coefficients, and wave excitation forces of the numerical models with and without nets.

The influence of the nets on the vessel's RAOs is primarily observed within the frequency range of 0.2-0.8 rad/s, with the most pronounced effects appearing in the surge, heave, and pitch motions. Reductions in wave forces at certain frequencies lead to corresponding decreases in motion responses after the nets are applied. Specifically, under head sea conditions, the surge motion RAO exhibits a noticeable drop near 0.69 rad/s, while the heave motion shows reductions near 0.40 rad/s and 0.68 rad/s. Under beam sea, the presence of the net leads to decreased RAOs for both surge and pitch motions around 0.65 rad/s. These reductions in RAOs can be clearly associated with noticeable decreases in the corresponding wave forces, and the wave forces are the dominant factor influencing the RAOs in these cases. In addition, there are several RAO peaks that decrease after the nets are applied, even though the corresponding wave excitation forces do not show a reduction. These include the surge and pitch motions near 0.40 rad/s under beam sea, and the pitch motion near 0.68 rad/s under head sea. These reductions in RAOs are attributed to the increased damping introduced by the nets. It is also noted that RAOs are particularly sensitive to damping variations near the natural frequencies.

For the effect on added mass, it can be observed from Figure 22 (b) that the application of the nets has only a minor effect in surge motion. However, for RAOs of heave and pitch motions in Figures 24 (b) and 26 (b), the nets have a more pronounced influence at frequencies above 0.40 rad/s, leading to a noticeable reduction in added mass. For this observation, the added mass in surge motion is primarily influenced by the hull geometry at the bow and stern, as well as the water inside the aquaculture tanks. As a result, the installation of the net structure has little effect on surge added mass. However, for heave and pitch motions, the dynamics involve water exchange between the tank interior and the surrounding fluid. After the net is applied, this exchange is weakened during motion, leading to a reduction in added mass.
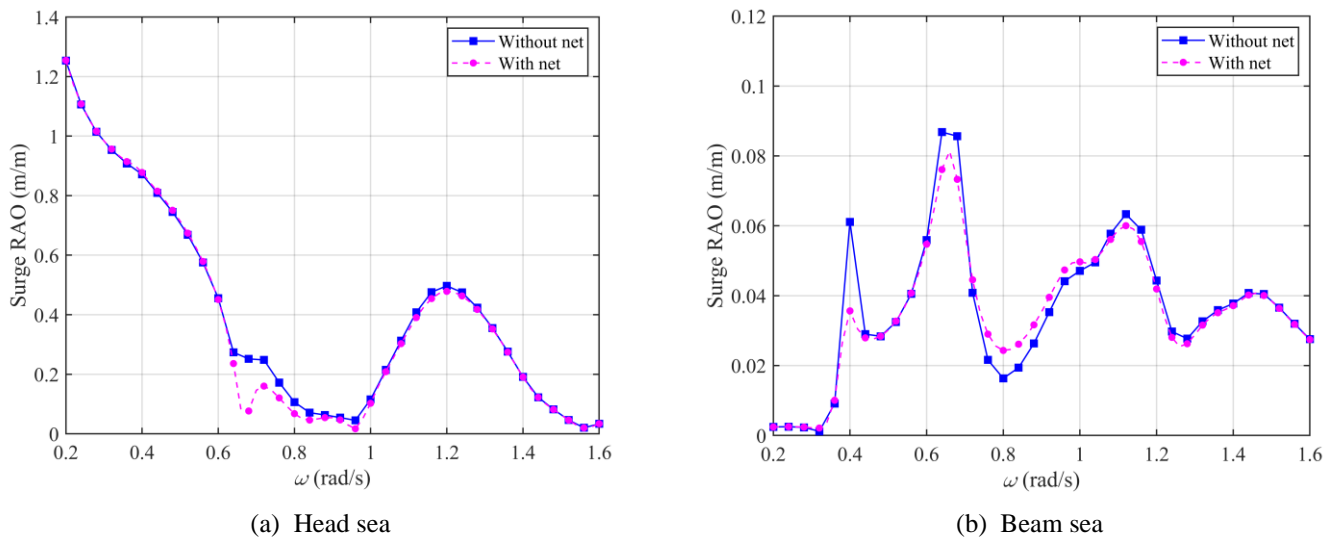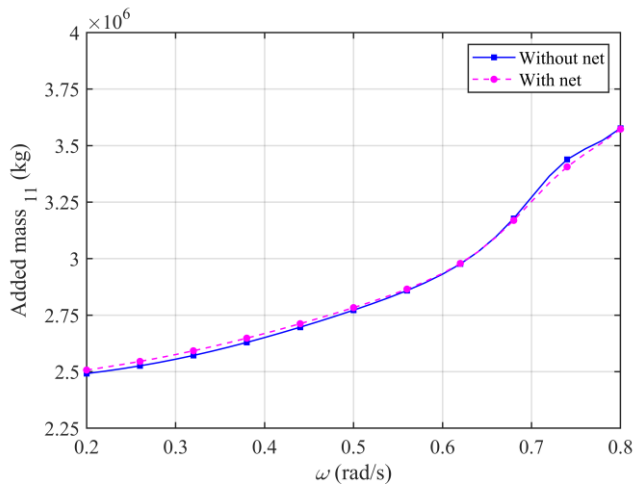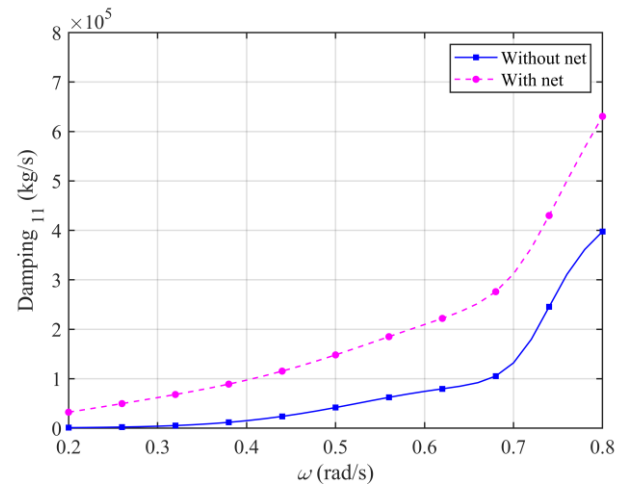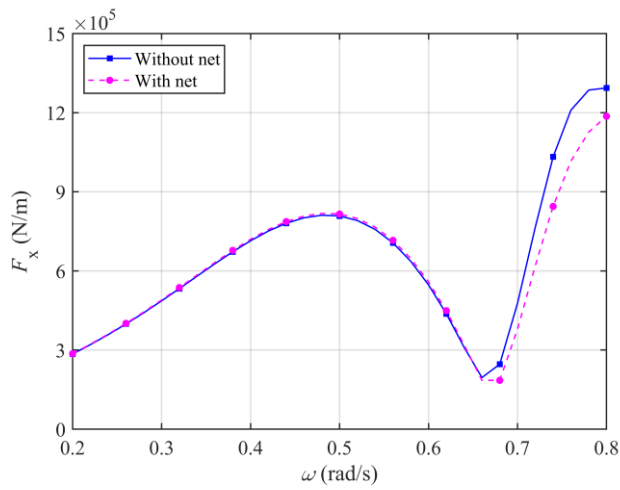

(a) Head sea   (b) Beam sea

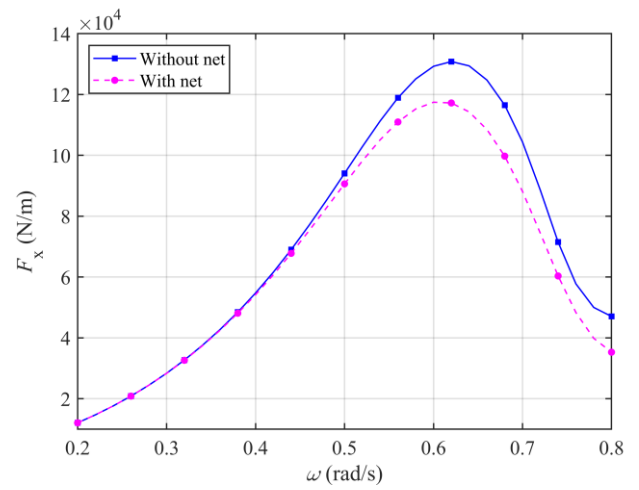**Fig. 22** The surge motion RAOs of the vessel with and without nets
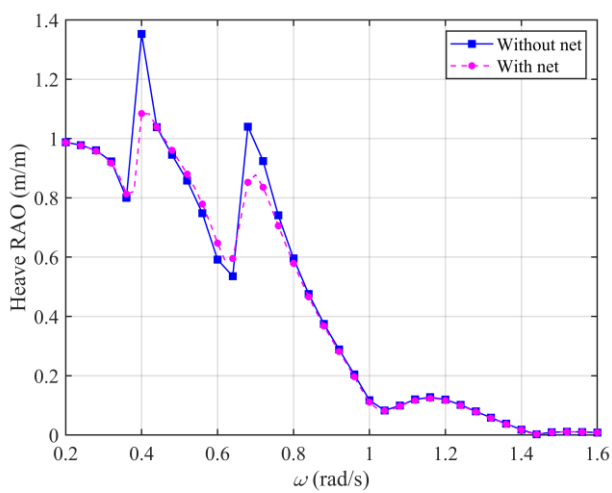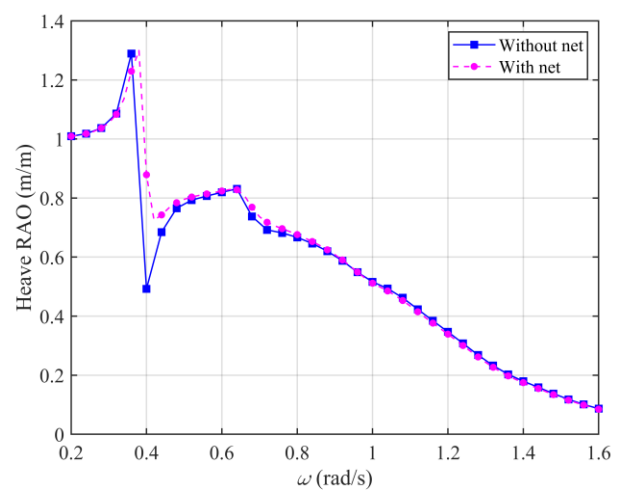
(a) Added mass

(b) Damping
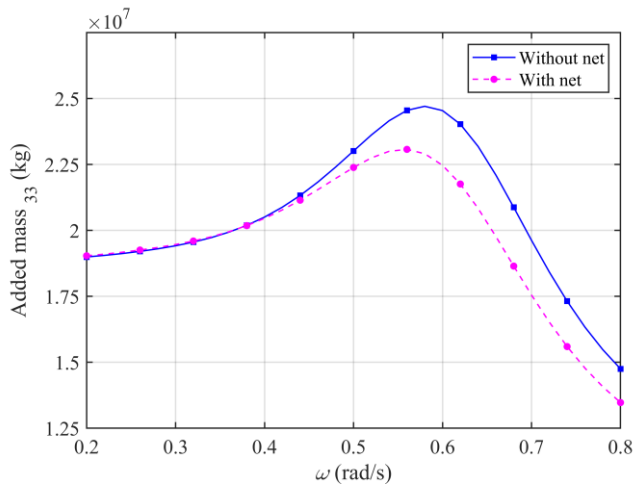
(d) Wave force (head sea)

(d) Wave force (beam sea)

Fig. 23 The hydrodynamic coefficients and wave force of surge motion of the vessel with and without nets
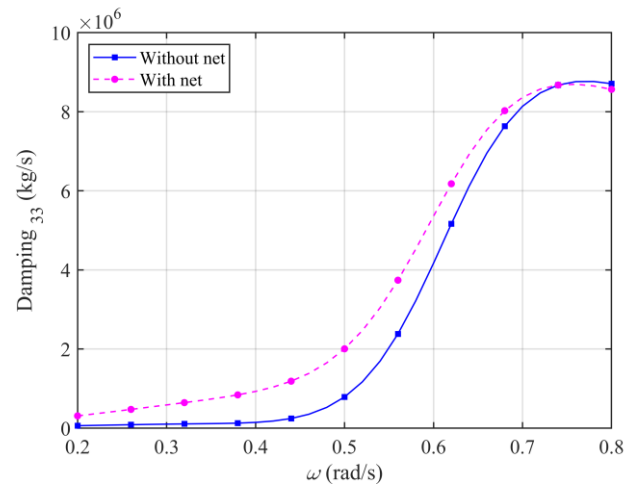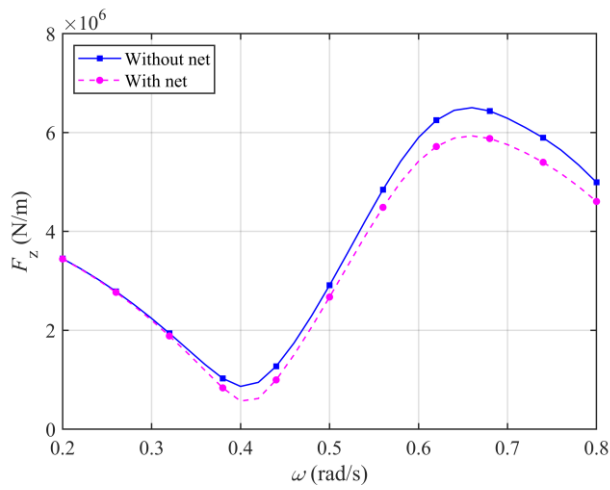

(a) Head sea

(b) Beam sea

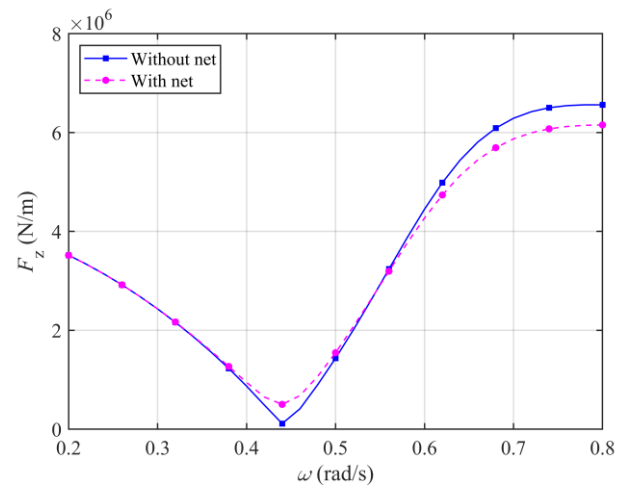**Fig. 24** The heave motion RAOs of the vessel with and without nets

(a) Added mass

(b) Damping

(d) Wave force (head sea)

(d) Wave force (beam sea)

Fig. 25 The hydrodynamic coefficients and wave force of heave motion of the vessel with and without nets

(a) Head sea

(b) Beam sea

Fig. 26 The pitch motion RAOs of the vessel with and without nets
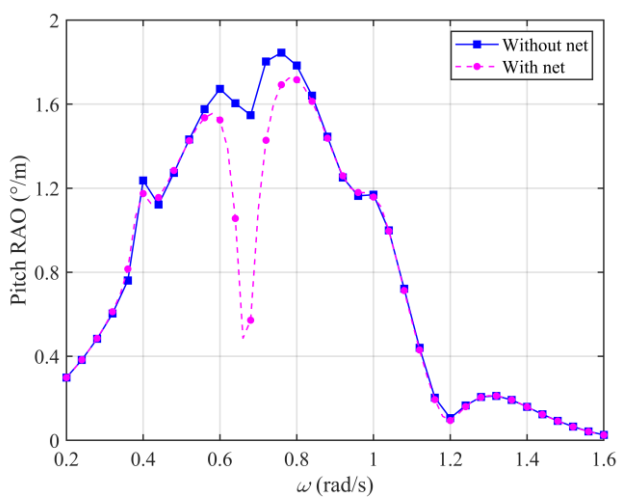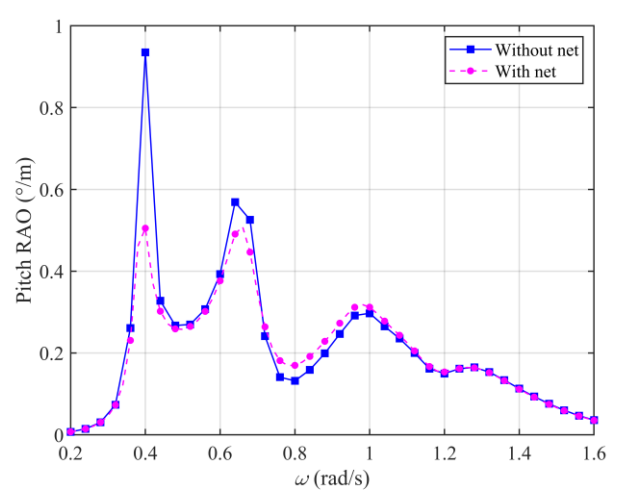
24

(a) Added mass

(b) Damping

(d) Wave force (head sea)
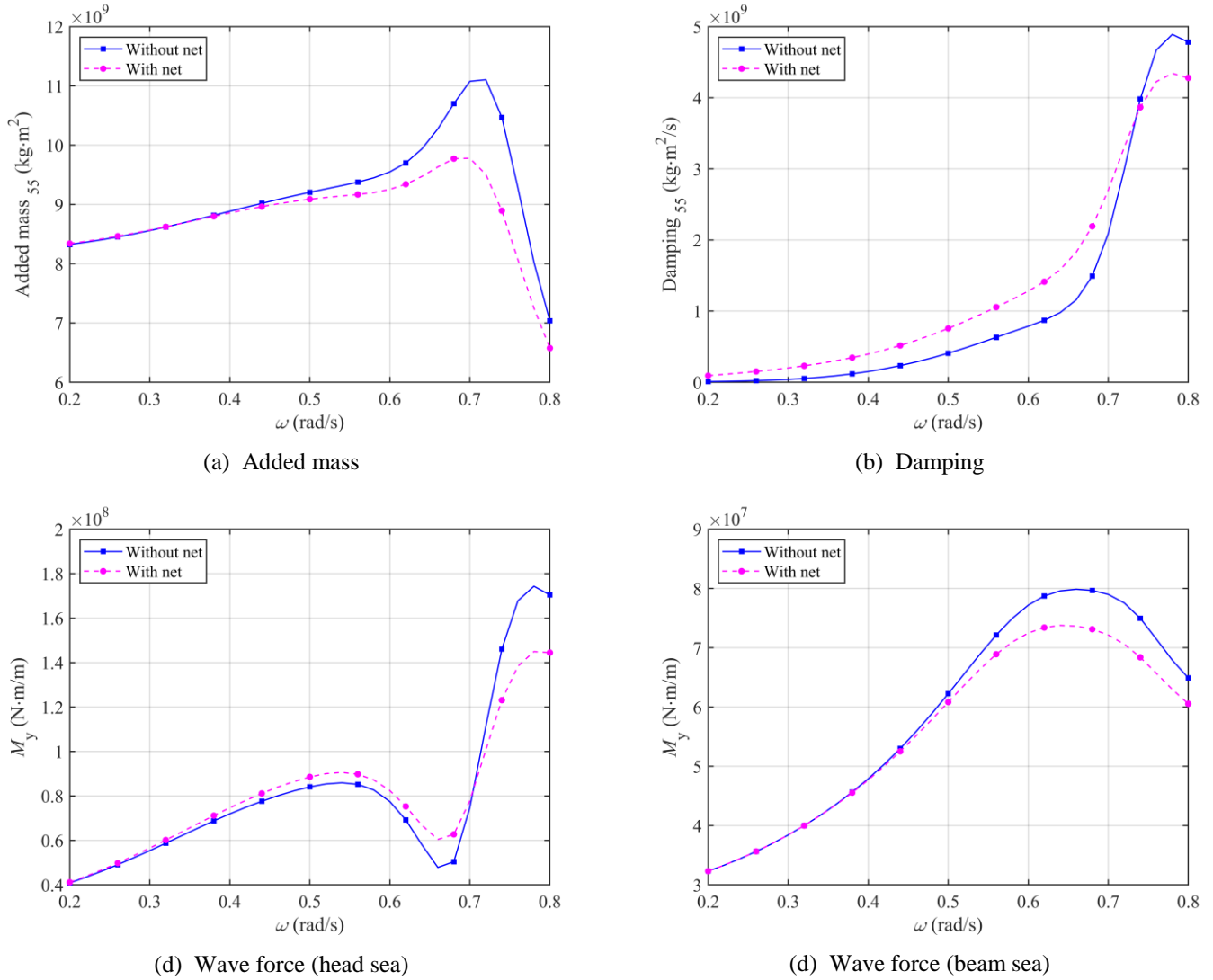
(d) Wave force (beam sea)

Fig. 27 The hydrodynamic coefficients and wave force of pitch motion of the vessel with and without nets

For damping, an overall increase is observed in surge, heave, and pitch motions after the application of the nets. Within the frequency range of 0.2-0.8 rad/s, the effect of the net on increasing the radiation damping is particularly significant. However, it can be observed that the increase in damping weakens as the frequency increases. In particular, for pitch motion under beam sea, the damping of the model with nets becomes smaller than that of the model without nets at frequencies above 0.72 rad/s. This observation is attributed to the decrease of discharge coefficient. As the frequency increases, the corresponding wavelength decreases, leading to an increase in wave slope ε. According to Equation (16), this results in a lower discharge coefficient b, indicating an increased resistance from the nets to the water exchange between the aquaculture tank and the surrounding fluid. This hindered exchange reduces the effectiveness of wave radiation, thereby leading to a decrease in radiation damping.
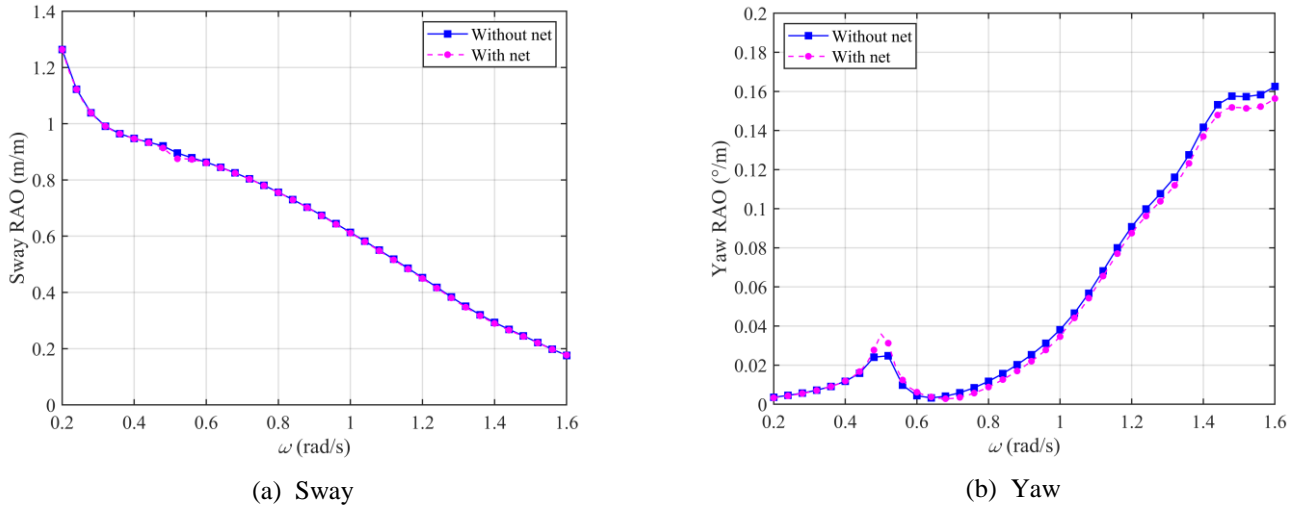
(a) Sway

(b) Yaw

Fig. 28 The sway and yaw motion RAOs of the vessel with and without nets
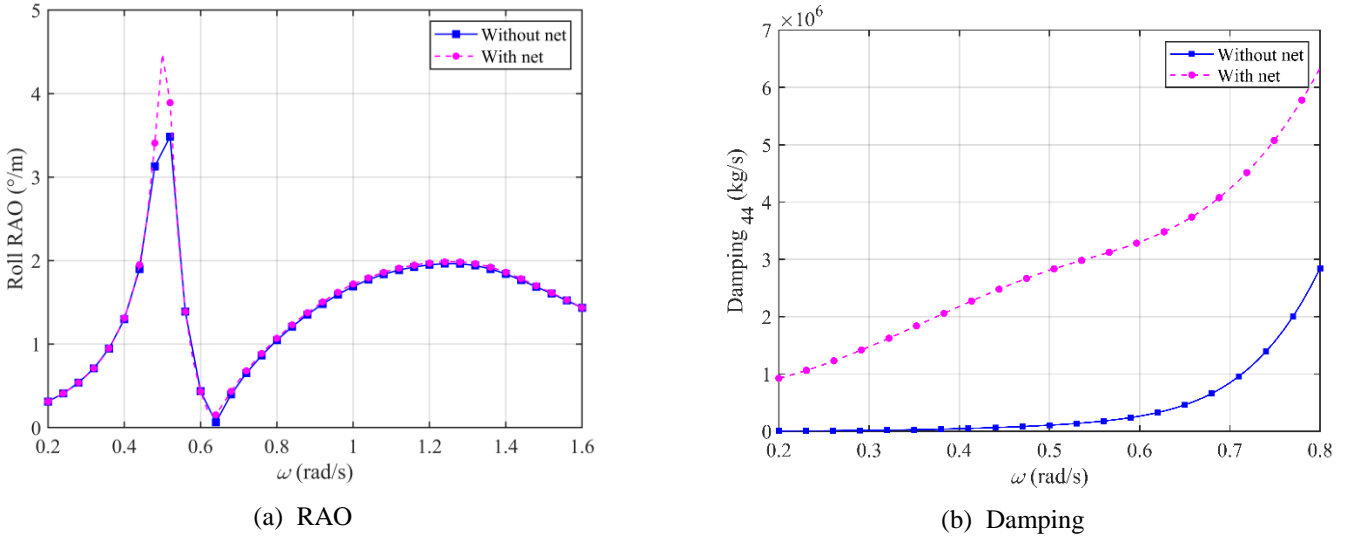

(a) RAO

(b) Damping

Fig. 29 The RAO and damping of the roll motion

For the three motions under beam wave conditions shown in Figure 27-28, it can be seen that the application of the nets has little impact on sway and yaw motions. However, for roll motion, the RAO peak near the natural frequency at 0.50 rad/s increases after the nets is applied. Considering that the installation of nets introduces additional damping, as illustrated in Figure 28 (b), the RAO around the natural frequency would normally be expected to decrease significantly under unchanged external excitation. However, the results indicate that after the nets were installed, the wave-induced moments on roll motion are increased. Furthermore, the influence of this increased excitation appears to outweigh the effect of the enhanced damping, leading to a higher RAO in the vicinity of the natural frequency. The effect of the increased excitation is greater than that of the added damping, which results in a higher RAO near the natural frequency.

4.3 Comparison between experimental and numerical results

In previous work, the seakeeping performance and dynamic motion responses of the novel fish farming vessel were investigated through physical model tests in wave basin. By comparing the experimental results with those of a bulk carrier, the superior seakeeping performance of the modified hull form were validated [8]. In this study, a numerical model consist of panel elements and dipole is employed to further analyse the seakeeping performance of the fish farming vessel. The numerical results are compared with experimental results obtained from free decay tests, regular wave tests, and white noise waves tests in this subsection,

thereby validating the accuracy of the proposed numerical model for evaluating the seakeeping performance of the novel fish farming vessel.

4.3.1   Free decay tests

Table 6 presents the natural frequencies and corresponding periods of the fish farming vessel for heave, roll, and pitch motions, obtained from both numerical simulations and physical experiments. The decay curves of heave, roll and pitch motions obtained from the free decay tests are presented in Figure 30. The natural periods in the numerical model were determined by solving an eigenvalue problem for the system. During both numerical and experimental analysis, it was observed that changing of the nets from NM1 to NM3 had no significant effect on the natural frequencies. Thus, only the results corresponding to net NM1 are discussed here.

A comparison between the numerical and experimental results shows that the natural frequencies for heave and roll motions are in close agreement, with relative error within 4%. However, for pitch motion, the natural frequency predicted by the numerical model is significantly higher than the experimental result, with a deviation of up to 40%. It is considered that this deviation is primarily attributed to the error in the model inertia moment used in the experiments. During the fabrication of the model and the adjustment of its center of gravity, part of the ballast was concentrated in the fore and aft regions, which likely resulted in a pitch moment of inertia larger than the scaled design value. This could lead to a significantly underestimation of the natural frequency measured in the experiments. In addition, in the numerical simulations, the neglect of the net volume effect could have caused an underestimation of the added mass, which would lead to an overestimation of the numerically predicted natural frequency. Besides, experimental observations revealed noticeable sloshing in the aquaculture tanks induced by pitch motion. Due to the openness of the nets, the internal sloshing also significantly influences the surrounding flow field. This interaction may not be fully captured in the numerical simulations, potentially resulting in an underestimation of the added mass associated with pitch motion.
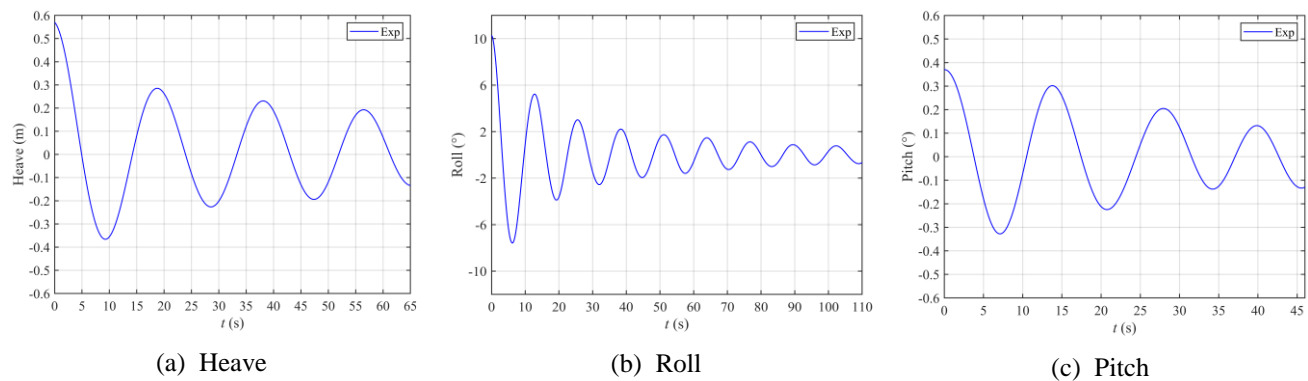

(a) Heave   (b) Roll   (c) Pitch

Fig. 30 The decay curves of fish farming vessel in free decay tests [8]

Table 6 The natural frequencies and periods of vessel

Degree of freedom	Heave		Roll		Pitch	
	Frequency (rad/s)	Period (s)	Frequency (rad/s)	Period (s)	Frequency (rad/s)	Period (s)
Num	0.39	16.07	0.51	12.34	0.69	9.08
Exp	0.34	18.85	0.49	12.81	0.49	13.03

4.3.2   Regular wave tests

The aim of regular wave tests is to verify the accuracy of the numerical RAO predictions, particularly in the frequency ranges where significant variations are observed. Therefore, the selected wave frequencies for the regular waves are concentrated around 0.40-0.70 rad/s and 0.90-1.10 rad/s. Figures 31 to 34 present a

comparison between the RAOs obtained from numerical simulations and those derived from regular wave experiments for different motion components. Since the amplitudes of yaw motions under beam sea are very small, they are not further analysed here.

For the experimental results corresponding to the three different net applications, the differences in the RAO are minor and show no clear relation between net solidity and motion response. This indicates that the variations in net solidity within the practical range have little influence on the motion responses of the fish farming vessel in the physical experiments. This observation is consistent with the numerical findings presented in the summery sentence at the beginning of Section 4.2.
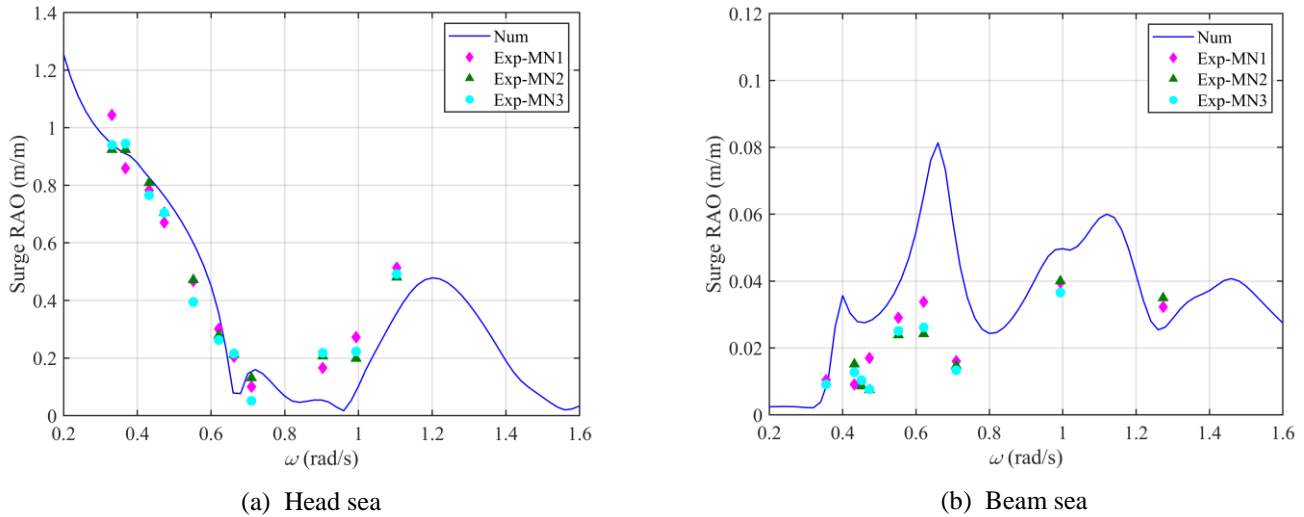
(a) Head sea	(b) Beam sea

Fig. 31 The surge motion RAOs of the numerical results and regular wave tests
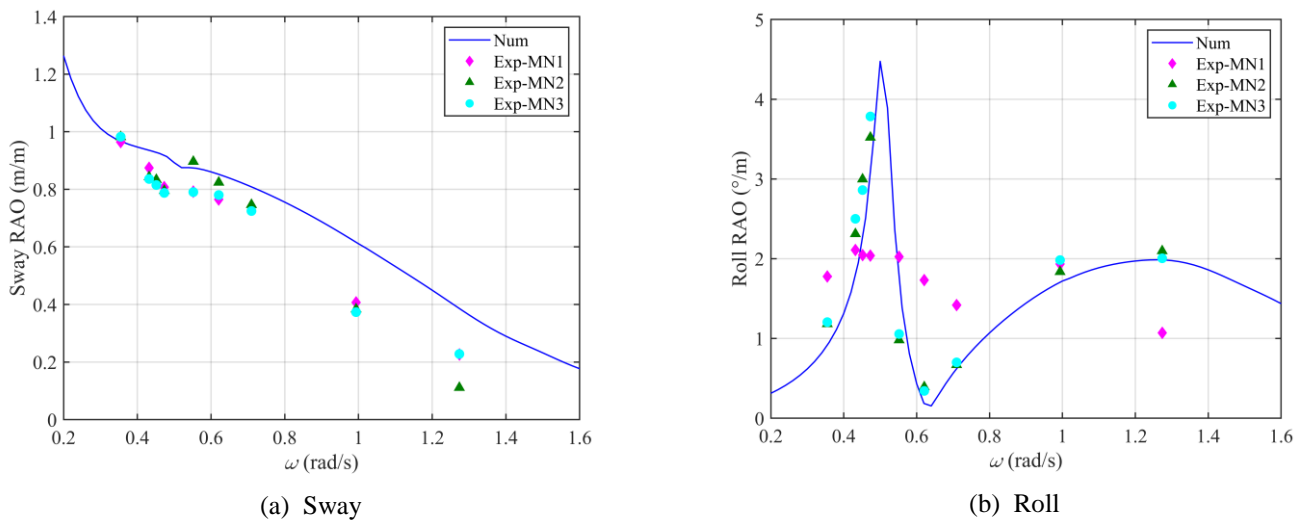
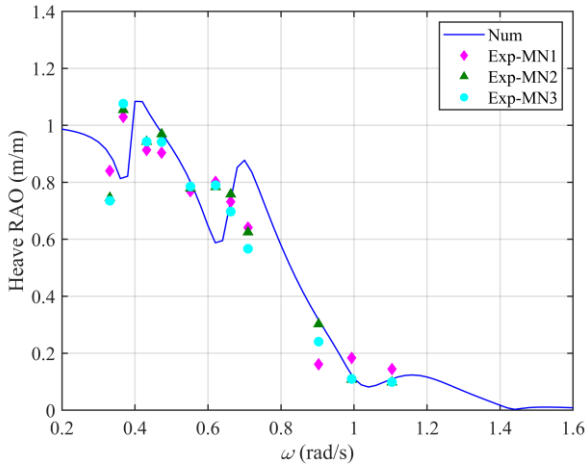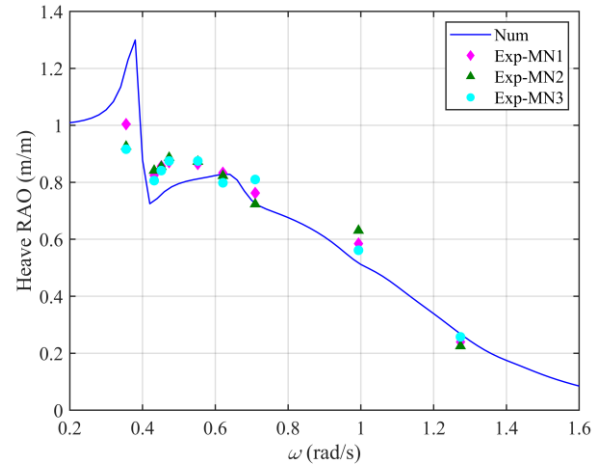| (a) Sway	(b) Roll

Fig. 32 The sway and roll motions RAOs of the numerical results and regular wave tests under beam sea

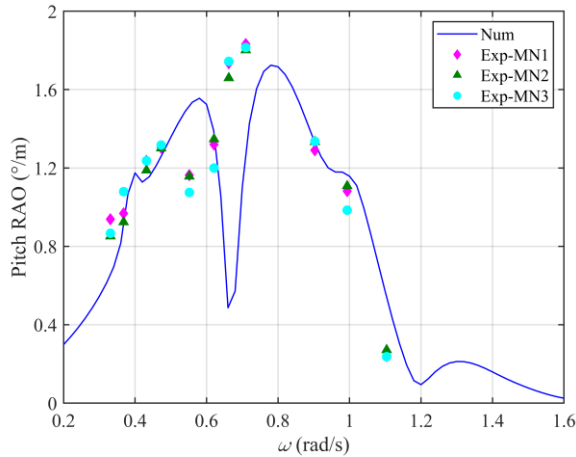(a) Head sea   (b) Beam sea

Fig. 33 The heave motion RAOs of the numerical results and regular wave tests

By comparing the experimental and numerical results in Figures 31-33, it is observed that the RAOs for surge, sway, heave, and roll motions show good agreement, indicating that the numerical model used in this study provides reliable predictions for these motions in the special frequency ranges. Notably, the difference between two types of results in surge motion under beam sea conditions is noticeable in Figure 31 (b). However, since the surge response is small in beam waves, the measurement is more susceptible to noise in experiments. Therefore, this difference is not further considered.

For the pitch motion results shown in Figure 34, differences can be observed between the numerical and experimental results in regions with significant variation of RAO. Under head sea conditions, the experimental results don't have a distinct trough near 0.69 rad/s like the trough in numerical result. Similarly, under beam sea conditions, no pronounced peak appears near 0.40 rad/s in the experimental data. These differences will be further analysed in the next subsection based on white noise tests, by comparing the continuous RAOs obtained from the physical tests and the numerical results.
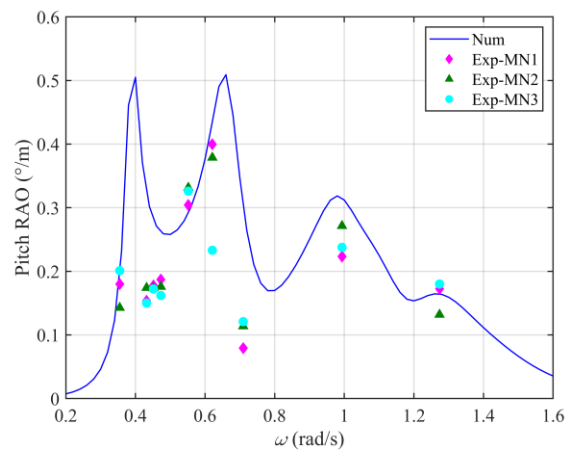
(a) Head sea   (b) Beam sea

Fig. 34 The pitch motion RAOs of the numerical results and regular wave tests

4.3.3   White noise waves tests

Although using regular waves to evaluate the motion responses at specific frequencies provides high accuracy, the discrete nature of the data limits its ability to capture the continuous trend of the response amplitude operator over the frequency range. Therefore, white noise waves tests are conducted in the experiment to obtain the continuous RAOs of the vessel, which are then compared with the numerical results.

The experimental data in this subsection are consistent with those used in the previous study by Zhang et al. [8].
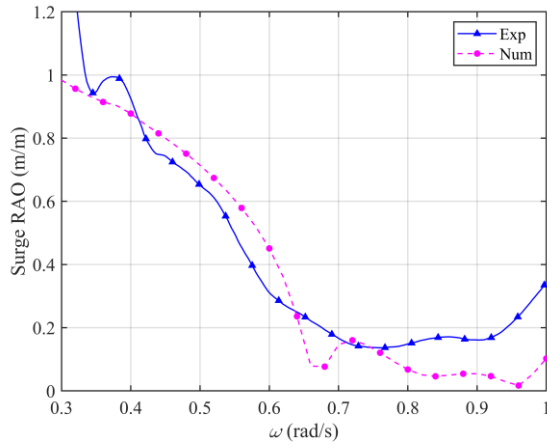
(a) Surge under head sea
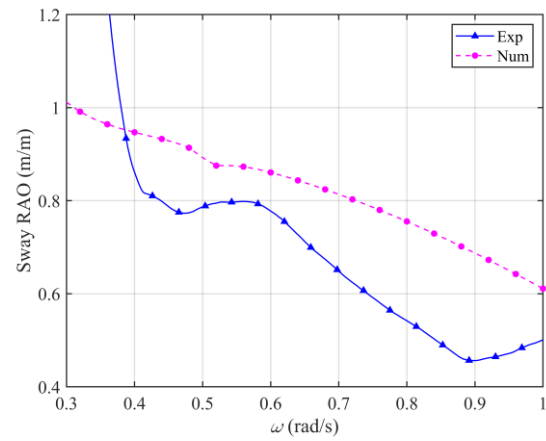
(b) Sway under beam sea

Fig. 35 The surge and sway motion RAOs of the numerical results and white noise waves tests

(a) Head sea

(b) Beam sea

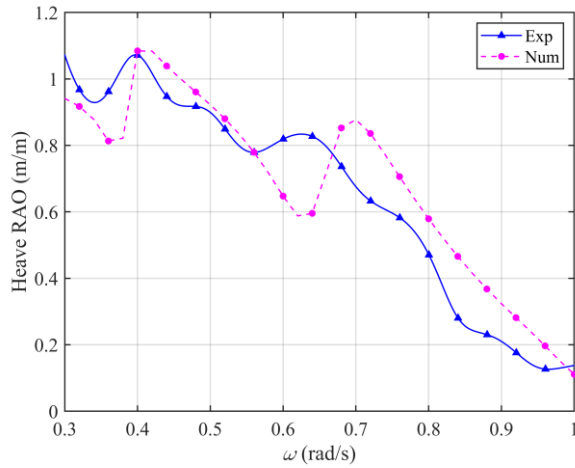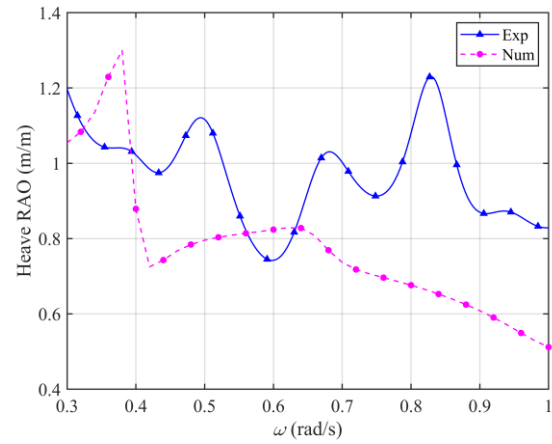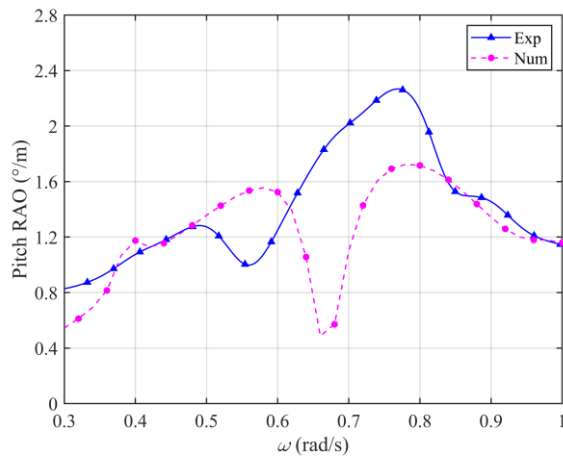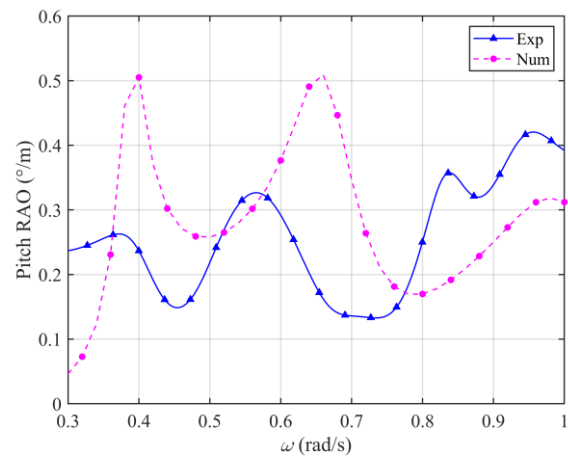**Fig. 36** The heave motion RAOs of the numerical results and white noise waves tests

(a) Head sea

(b) Beam sea

Fig. 37 The pitch motion RAOs of the numerical results and white noise waves tests
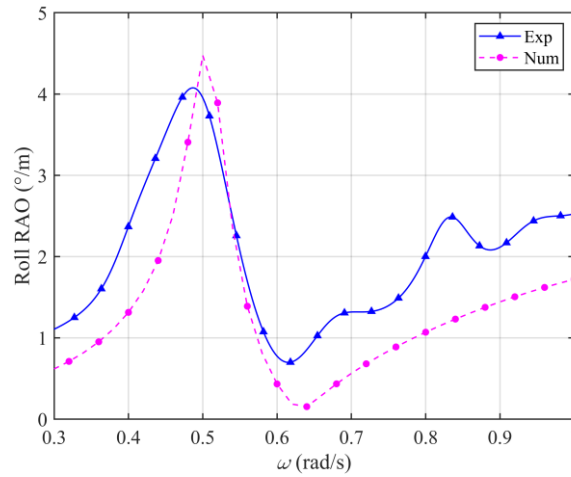
Fig. 38 The roll motion RAOs of the numerical results and white noise waves tests

Figures 35-38 present the comparisons between the RAOs obtained from numerical simulations and those derived from the white noise tests for different motion components. Here, attention is focused on the wave headings where the motion responses are more significant. Thus, only head sea results are analysed for surge motion, and only beam sea results for sway and roll motions. For pitch and heave motions, both wave headings are considered.

Overall, the RAOs obtained from numerical simulations show a generally good agreement with the experimental results in terms of variation trends. Some specific seakeeping characteristics of the vessel, which were observed during experiments, are also reflected in the numerical results. This is particularly evident in the pitch motion under head sea conditions, where both the numerical and experimental results exhibit a peak near 0.79 rad/s. This peak is considered to correspond to a high-frequency natural period of pitch motion, which arises due to the similarity in hull form between the modified vessel and the original bulk carrier. In addition, both numerical and experimental results show troughs near 0.68 rad/s and 0.57 rad/s, respectively, which are believed to result from the suppressive effect of longitudinal tank sloshing on the pitch motion. The detail has been discussed in previous studies [8].

However, the results show that there is a frequency shift between the numerical and experimental data. Although the overall trends of the numerical results are consistent with those of the experimental results, the corresponding frequencies of the numerical results are generally higher. For example, in the case of heave motion under head sea in Figure 36 (a), the two peak values in the numerical results appear near 0.40 rad/s and 0.70 rad/s, while the corresponding peaks are observed near 0.38 rad/s and 0.64 rad/s in the experimental results. For pitch motion in Figure 37, both the numerical and experimental results exhibit a trend of increasing, then decreasing, and increasing again, but the numerical results clearly show a higher frequency shift compared to the experimental ones. Similarly, the frequency shift of the peak in the roll motion is more evident in Figure 38. It can also be observed that these peak values correspond to the vessel's natural frequencies. This observation is primarily attributed to the underestimation of the added mass in the numerical simulations. The omission of the nets' volume and the influence of mesh resolution on the radiation potential solution in the numerical model lead to an underestimation of the added mass, which in turn results in an overestimation of the natural frequencies.

In addition, the coupling between different degrees of freedom is less evident in the numerical simulations compared to the experimental results. For example, in the case of heave motion under beam sea in Figure 36 (b), the experimental results reveal the coupling effects with roll motion near 0.50 rad/s and the higher-frequency natural period of pitch motion near 0.82 rad/s. However, the numerical results only capture the natural frequency of heave motion near 0.39 rad/s, with no significant indication of coupling with other modes. This is considered to be caused by the limitations of the potential flow theory used in the numerical simulations, which may not accurately capture the coupling effects induced by large-amplitude motions and viscous forces [49, 50]. During the experiments, sloshing in the liquid tanks and mild overtopping were

observed as illustrated in Figure 39, both of which contribute to the increased nonlinearity of the vessel's motion.
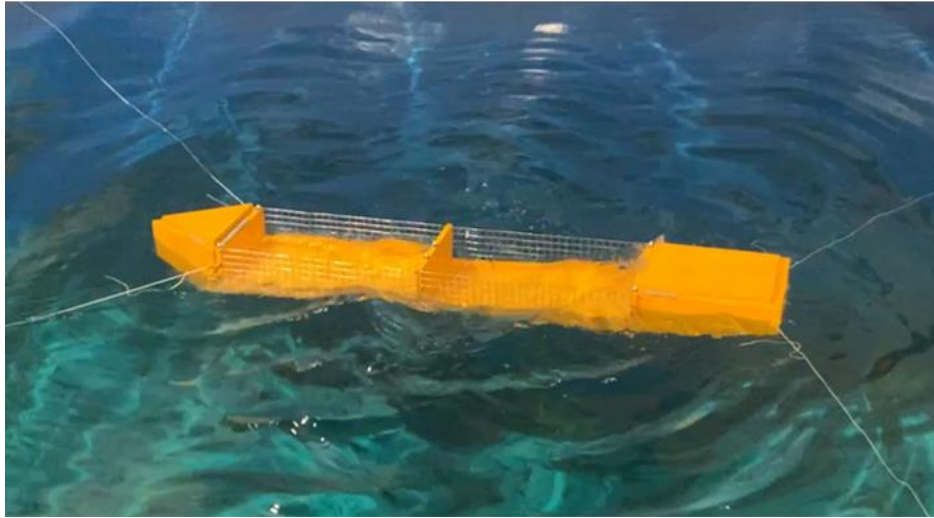

Fig. 39 Sloshing and overtopping in aquaculture tanks under head sea [8]

5. Conclusions

This study investigates the seakeeping performance of a novel fish farming vessel through both numerical simulations and physical experiments. In the numerical analysis, the metal nets are modeled using dipole elements, and the overall vessel is represented by a combination of dipole and panel elements. The influence of significant variations in the discharge coefficient on the RAOs of different degrees of freedom is examined, and reliable numerical results for the vessel's seakeeping performance and hydrodynamic parameters are obtained. The impact of the nets on seakeeping behaviour and hydrodynamic coefficients is further analysed by comparing models with and without nets. Finally, the numerical results are validated against experimental results, confirming the effectiveness of the proposed method while also identifying its limitations. The conclusions are summarized as follows:

- The proposed numerical method is capable of simulating the seakeeping performance of the novel fish farming vessel, and the predicted trends show good agreement with the experimental results. Using dipole elements to numerically model the metal nets is shown to be a feasible approach. Moreover, it is necessary to account for the influence of frequency-dependent wave slope on the porosity-related discharge coefficient of the dipole elements, as this variation can significantly affect the accuracy of the numerical results.

- When the porosity of the net structure varies within the typical range of engineering applications, its influence on the vessel's seakeeping performance remains minor from both numerical and experimental analysis.

- The frequency-dependent variation of wave slope leads to significant changes in the discharge coefficient of the nets in numerical model. This has a considerable impact on the seakeeping performance of the vessel, with the exception of sway and yaw motions. The influence is primarily concentrated near the natural frequencies within the range of 0.2-1.0 rad/s, where the RAO peak values generally increase with larger discharge coefficients.

- The primary impact of the nets lies in the RAO peaks near the natural frequencies in the numerical modeling. After the net is applied, the RAOs generally decrease around these frequencies due to a reduction in wave excitation forces and an increase in damping composed of both wave-radiation damping and the damping arised from energy dissipation. An exception is observed in the roll motion, where the RAO near the natural frequency increases after the net is installed. This is attributed to the enhanced wave-induced moment in the roll motion, which outweighs the damping

effect, resulting in a higher roll response.

- The RAO trends obtained from simulations match well with those observed in the experiments, particularly for heave and roll motions. However, the underestimation of added mass leads to a shift in natural frequencies, especially for pitch motion. In the present numerical model, a linear formulation was adopted for the pressure drop across the nets in order to improve computational efficiency. Future refinements will involve employing a quadratic relation for the pressure drop with iterative calculations to enhance accuracy. In addition, inertial effects could also be incorporated into the model.

ACKNOWLEDGMENTS

FUNDING

REFERENCES

[1]   DET NORSKE VERITAS, DNV, 2021. Marine Aquaculture Forecast. https://www.dnv.com/focus-areas/offshore-aquaculture/marine-aquaculture-forecast/ (accessed 5st August 2025)

[2]   Gulpinar, J.,2021. Analysis of the Havfarm concept for extreme environ-mental loads. *Master Thesis*, Norwegian University of Science and Technology, Gløshaugen, Trondheim, Trøndelag, Norway.

[3]   Zheng，C.，2025. Innovative vessel in Guangdong signals new era sea farming. https://global.chinadaily.com.cn/a/202505/29/WS6837b31da310a04af22c2218.html (accessed 5st August 2025)

[4]   Godfrey, M., 2025. Guoxin launches new and improved deep-sea aquaculture vessel, with several more on the way. https://www.seafoodsource.com/news/aquaculture/guoxin-launches-new-and-improved-deep-sea-aquaculture-vessel-with-several-more-on-the-way (accessed 5st August 2025)

[5]   Hui, L., Sun, Z., Han, B., Shao, Y., Deng, B., 2022. Research on the motion response of aquaculture ship and tank sloshing under rolling resonance. *Brodogradnja*, 73(2), 1-15. https://doi.org/10.21278/brod73201

[6]   Jia, G., Jiao, J., Chen, C., Wu, T., 2025. CFD simulation of wave-induced motions of an LNG ship considering tank sloshing effects. *Brodogradnja*, 76(3), 1-27. https://doi.org/10.21278/brod76307

[7]   Dixon, G., 2025. Old capesizes wanted as China unveils first bulker converted into aquaculture ship. https://www.tradewindsnews.com/shipyards/old-capesizes-wanted-as-china-unveils-first-bulker-converted-into-aquaculture-ship/2-1-1848686 (accessed 5st August 2025)

[8]   Zhang, J., Liu, Z., Chen, W., Huang, W., Li, B., 2025. Experimental study on seakeeping and dynamic motion performance of a novel concept of fish farming vessel. *Ocean Engineering* 332, 121469. https://doi.org/10.1016/j.oceaneng.2025.121469

[9]   Li, B., Ou, J., Teng, B., 2010. Fully coupled effects of hull, mooring and risers model in time domain based on an innovative deep draft multi-spar. *China Ocean Engineering*, 24, 219-233.

[10]   Li, B., Ou, J., 2009. Heave response analysis of Truss Spar in frequency domain. *The Ocean Engineering*, 27(1), 8-15.

[11]   Jian, W., Cao, D., Lo, E. Y., Huang, Z., Chen, X., Cheng, Z., Gu, H., Li, B., 2017. Wave runup on a surging vertical cylinder in regular waves. *Applied Ocean Research*, 63, 229-241. https://doi.org/10.1016/j.apor.2017.01.016

[12]   Wang, X., Qiao, D., Jin, L., Yan, J., Wang, B., Li, B., Ou, J., 2023. Numerical investigation of wave run-up and load on heaving cylinder subjected to regular waves. *Ocean Engineering*, 268, 113415. https://doi.org/10.1016/j.oceaneng.2022.113415

[13]   Lee, C. W., Lee, J. H., Cha, B. J., Kim, H. Y., Lee, J. H., 2005. Physical modeling for underwater flexible systems dynamic simulation. *Ocean Engineering*, 32(3-4), 331-347. https://doi.org/10.1016/j.oceaneng.2004.08.007

[14]   Kristiansen, T., Faltinsen, O. M., 2012. Modelling of current loads on aquaculture net cages. *Journal of Fluids and Structures*, 34, 218-235. https://doi.org/10.1016/j.jfluidstructs.2012.04.001

[15]   Kawakami, T., 1964. The theory of designing and testing fishing nets in model. *Modern Fishing Gear of the World*, 2, 471-482.

[16] Takagi, T., Shimizu, T., Suzuki, K., Hiraishi, T., Yamamoto, K., 2004. Validity and layout of "NaLA": a net configuration and loading analysis system. *Fisheries Research*, 66(2-3), 235-243. https://doi.org/10.1016/S0165-7836(03)00204-2

[17] Moe-Føre, H., Christian Endresen, P., Gunnar Aarsæther, K., Jensen, J., Føre, M., Kristiansen, D., Reite, K. J., 2015. Structural analysis of aquaculture nets: comparison and validation of different numerical modeling approaches. *Journal of Offshore Mechanics and Arctic Engineering*, 137(4), 041201. https://doi.org/10.1115/1.4030255

[18] Bai, X., Lu, Z., Luo, H., Guo, M., Yang, C., 2025. Experimental and numerical investigations on hydrodynamic response of vessel-shaped semi-submersible aquacultural platform. *Aquacultural Engineering*, 110, 102540. https://doi.org/10.1016/j.aquaeng.2025.102540

[19] Li, L., Jiang, Z., Høiland, A. V., Ong, M., 2018. Numerical analysis of a vessel-shaped offshore fish farm. *Journal of Offshore Mechanics and Arctic Engineering*, 140(4), 041201. https://doi.org/10.1115/1.4039131

[20] Chen, M., Huang, W., Liu, H., Hallak, T. S., Liu, S., Yang, Y., Tao, T., Jiang, Y., 2025. A novel SPM wind-wave-aquaculture system: Concept design and fully coupled dynamic analysis. *Ocean Engineering*, 315, 119798. https://doi.org/10.1016/j.oceaneng.2024.119798

[21] Jin, J., Su, B., Dou, R., Luan, C., Li, L., Nygaard, I., Fonseca, N., Gao, Z., 2021. Numerical modelling of hydrodynamic responses of Ocean Farm 1 in waves and current and validation against model test measurements. *Marine Structures*, 78, 103017. https://doi.org/10.1016/j.marstruc.2021.103017

[22] Miao, Y., Ding, J., Tian, C., Chen, X., Fan, Y., 2021. Experimental and numerical study of a semi-submersible offshore fish farm under waves. *Ocean Engineering*, 225, 108794. https://doi.org/10.1016/j.oceaneng.2021.108794

[23] Shi, L., 2019. Dynamic analysis of semi-submersible offshore fish farm operated in China East Sea. Master Thesis, *Master Thesis*, Norwegian University of Science and Technology, Gløshaugen, Trondheim, Trøndelag, Norway.

[24] Cheng, H., Li, L., Aarsæther, K. G., Ong, M., 2020. Typical hydrodynamic models for aquaculture nets: A comparative study under pure current conditions. *Aquacultural Engineering*, 90, 102070. https://doi.org/10.1016/j.aquaeng.2020.102070

[25] Liu, J., Li, B., 2025. A deep learning model for predicting mechanical behaviors of dynamic power cable of offshore floating wind turbine. *Marine Structures*, 99, 103705. https://doi.org/10.1016/j.marstruc.2024.103705

[26] Molin, B., 2011. Hydrodynamic modeling of perforated structures. *Applied Ocean Research*, 33(1), 1-11. https://doi.org/10.1016/j.apor.2010.11.003

[27] Li, B., Huang, W., Chen, X., 2018. A numerical study of dynamic response of crane semi-submersible along TLP in tender-assisted drilling operation. *Ships and Offshore Structures*, 13(sup1), 273-286. https://doi.org/10.1080/17445302.2018.1446707

[28] Li, B., Liu, Z., Liang, H., Zheng, M., Qiao, D., 2023. BEM modeling for the hydrodynamic analysis of the perforated fish farming vessel. *Ocean Engineering*, 285, 115225. https://doi.org/10.1016/j.oceaneng.2023.115225

[29] Qiao, D., Feng, C., Yan, J., Liang, H., Ning, D., Li, B., 2020. Numerical simulation and experimental analysis of wave interaction with a porous plate. *Ocean Engineering*, 218, 108106. https://doi.org/10.1016/j.oceaneng.2020.108106

[30] Qiao, D., Mackay, E., Yan, J., Feng, C., Li, B., Feichtner, A., Ning, D., Johanning, L., 2021. Numerical simulation with a macroscopic CFD method and experimental analysis of wave interaction with fixed porous cylinder structures. *Marine Structures*, 80, 103096. https://doi.org/10.1016/j.marstruc.2021.103096

[31] Tian, Z., Yang, H., Wen, H., 2024. Hydrodynamic performance of a submersible net cage integrated with an offshore platform. *Frontiers in Marine Science*, 11, 1436992. https://doi.org/10.3389/fmars.2024.1436992

[32] Liu, Q., Chen, H., Wang, B., 2024. A true double-body method based on porous media model for simulation and Froude scaling verification of an aquaculture vessel resistance. *Ocean Engineering*, 310, 118501. https://doi.org/10.1016/j.oceaneng.2024.118501

[33] Li, B., Wang, C., 2023. The absolute nodal coordinate formulation in the analysis of offshore floating operations Part I: Theory and modeling. *Ocean Engineering*, 281, 114645. https://doi.org/10.1016/j.oceaneng.2023.114645

[34] Wang, C., Liu, J., Li, B., Huang, W., 2023. The absolute nodal coordinate formulation in the analysis of offshore floating operations, Part II: Code validation and case study. *Ocean Engineering*, 281, 114650. https://doi.org/10.1016/j.oceaneng.2023.114650

[35] Qiao, D., Li, B., Yan, J., Qin, Y., Liang, H., Ning, D., 2021. Transient responses evaluation of FPSO with different failure scenarios of mooring lines. *Journal of Marine Science and Engineering*, 9(2), 103. https://doi.org/10.3390/jmse9020103

[36] Zhang, Y., Han, Z., Zhou, X., Li, B., Zhang, L., Zhen, E., Wang, S., Zhao, Z., Guo, Z., 2023. METO-S2S: A S2S based vessel trajectory prediction method with Multiple-semantic Encoder and Type-Oriented Decoder. *Ocean Engineering*, 277, 114248. https://doi.org/10.1016/j.oceaneng.2023.114248

[37] Liang, H., Chen, X., 2025. Boundary element method for wave interactions with marine structures: From conventional to emerging applications. *Engineering Analysis with Boundary Elements*, 179, 106326. https://doi.org/10.1016/j.enganabound.2025.106326

[38]   Ouled Housseine, C., Malenica, S., De Hauteclocque, G., Chen, X.-B., 2018. Hydrodynamic Interactions of the Truncated Porous Vertical Circular Cylinder With Water Waves. *International Conference on Offshore Mechanics and Arctic Engineering (OMAE2018)*, Volume 9, 17–22 June, Madrid, Spain. https://doi.org/10.1115/OMAE2018-78221

[39]   Mackay, E., Liang, H., Johanning, L., 2021. A BEM model for wave forces on structures with thin porous elements. *Journal of Fluids and Structures*, 102, 103246. https://doi.org/10.1016/j.jfluidstructs.2021.103246

[40]   Wehausen, J.V., Laitone, E.V., 1960. Surface waves. In: Fluid Dynamics. *Springer*, Berlin, Heidelberg, pp. 446–778. https://doi.org/10.1007/978-3-642-45944-3_6

[41]   Li, B., 2021. Effect of hydrodynamic coupling of floating offshore wind turbine and offshore support vessel. A*pplied Ocean Research*, 114, 102707. https://doi.org/10.1016/j.apor.2021.102707

[42]   Liang, H., Ouled Housseine, C., Chen, X., Shao, Y., 2020. Efficient methods free of irregular frequencies in wave and solid/porous structure interactions. *Journal of Fluids and Structures*, 98, 103130. https://doi.org/10.1016/j.jfluidstructs.2020.103130

[43]   Bureau Veritas, BV, 2022. Hydrostar for Experts User Manual. *Research Department of Bureau Veritas*, Paris, France.

[44]   Huang, W., Li, B., Chen, X., 2023. A new quasi-dynamic method for the prediction of tendon tension of TLP platform. *Ocean Engineering*, 270, 113590. https://doi.org/10.1016/j.oceaneng.2022.113590

[45]   Li, B., Liang, H., Chen, X., Araujo, R., 2021. Study of telescopic gangway motions in time domain during offshore operation. *Ocean Engineering*, 230, 108692. https://doi.org/10.1016/j.oceaneng.2021.108692

[46]   Yang, L., Li, B., Zhang, K., Duan, M., Chen, X., 2025. Investigation of global and local structural response of Semi-submersible FOWT using hydro-structure interaction in the frequency domain. *Applied Ocean Research*, 154, 104318. https://doi.org/10.1016/j.apor.2024.104318

[47]   Liang, H., Shao, Y., Chen, J., 2021. Higher-order derivatives of the Green function in hyper-singular integral equations. *European Journal of Mechanics - B/Fluids*, 86, 223-230. https://doi.org/10.1016/j.euromechflu.2020.12.006

[48]   Zhao, F., Bao, W., Kinoshita, T., Itakura, H., 2010. Theoretical and experimental study on a porous cylinder floating in waves. *Journal of Offshore Mechanics and Arctic Engineering*, 133(1), 011301. https://doi.org/10.1115/1.4001435

[49]   Phuong, N. T. H., Taniguchi, T., Katayama, T., 2025. Numerical study of scale effects of viscous roll damping for a container ship. *Brodogradnja*, 76(4), 76406. https://doi.org/10.21278/brod76406

[50]   Yang, L., Li, B., Dong, Y., Hu, Z., Zhang, K., Li, S., 2025. Large-amplitude rotation of floating offshore wind turbines: A comprehensive review of causes, consequences, and solutions. *Renewable and Sustainable Energy Reviews*, 211, 115295. https://doi.org/10.1016/j.rser.2024.115295